ARTICLE

Polarized localization of kinesin-1 and RIC-7 drives axonal mitochondria anterograde transport

Youjun Wu[1,2], Chen Ding[1,2], Behrang Sharif[3,4], Alexis Weinreb[1,2], Grace Swaim[2], Hongyan Hao[2], Shaul Yogev[2], Shigeki Watanabe[3,4], and Marc Hammarlund[1,2]

Mitochondria transport is crucial for axonal mitochondria distribution and is mediated by kinesin-1-based anterograde and dynein-based retrograde motor complexes. While Miro and Milton/TRAK were identified as key adaptors between mitochondria and kinesin-1, recent studies suggest the presence of additional mechanisms. In *C. elegans*, *ric-7* is the only single gene described so far, other than kinesin-1, that is absolutely required for axonal mitochondria localization. Using CRISPR engineering in *C. elegans*, we find that Miro is important but is not essential for anterograde traffic, whereas it is required for retrograde traffic. Both the endogenous RIC-7 and kinesin-1 act at the leading end to transport mitochondria anterogradely. RIC-7 binding to mitochondria requires its N-terminal domain and partially relies on MIRO-1, whereas RIC-7 accumulation at the leading end depends on its disordered region, kinesin-1, and metaxin2. We conclude that transport complexes containing kinesin-1 and RIC-7 polarize at the leading edge of mitochondria and are required for anterograde axonal transport in *C. elegans*.

Introduction

Mitochondria are complex organelles with multiple functions including ATP production, calcium buffering, reactive oxygen species signaling, and programmed cell death. In neurons, synaptic mitochondria support neurotransmission by at least two mechanisms: serving as an energy source via ATP production, and acting as a reservoir for calcium buffering (Ivannikov et al., 2013; Kang et al., 2008; Kwon et al., 2016; Sun et al., 2013; Tang and Zucker, 1997; Verstreken et al., 2005). Therefore, maintaining mitochondria distribution is critical for neuronal homeostasis. Indeed, mitochondria mislocalization can lead to neurodegeneration, and defects in mitochondria trafficking are found in a variety of disease models for Alzheimer's disease, Parkinson's disease, and amyotrophic lateral sclerosis (Baldwin et al., 2016; De Vos et al., 2007; Ding et al., 2022; López-Doménech et al., 2016; Nguyen et al., 2014; Rawson et al., 2014; Rui et al., 2006; Wang et al., 2010, 2011; Zhao et al., 2010).

Although evidence suggests that mitochondria biogenesis can occur in the axon, it is believed that most mitochondria are generated in the cell body and transported to distal processes (Amiri and Hollenbeck, 2008; Davis and Clayton, 1996). Mitochondria transport is primarily driven by the microtubule plus-end–directed motor kinesin-1 and the minus-end–directed motor dynein (Hurd and Saxton, 1996; Pilling et al., 2006).

Microtubules in the axon are predominantly oriented with their plus end pointing toward the distal tip (plus-end-out). Therefore, kinesin-1 mainly drives the exit of mitochondria from the cell body into the axon and anterograde trafficking toward the distal end, whereas dynein moves mitochondria retrogradely in the axon toward the cell body.

The kinesin-1 and dynein motors bind mitochondria through adaptor complexes, such as Miro and Milton/TRAK (Amiri and Hollenbeck, 2008; Glater et al., 2006; Guo et al., 2005; Stowers et al., 2002; van Spronsen et al., 2013). Miro is a conserved GTPase with a C-terminal transmembrane domain that inserts into the outer mitochondria membrane (Fransson et al., 2003). Miro binds to Milton, a coiled-coil protein that in turn binds to kinesin-1 and to dynein (Glater et al., 2006; van Spronsen et al., 2013). In vitro, Miro can also bind to KIF5/kinesin-1 directly (Macaskill et al., 2009). In *Drosophila* photoreceptors and motor neurons, loss-of-function of either Miro or Milton leads to dramatic loss of mitochondria in axons and depletion of mitochondria at the neuromuscular junctions, suggesting that Miro and Milton are essential for mitochondria exit from the cell body and axonal anterograde traffic (Guo et al., 2005; Stowers et al., 2002). In mice, Miro1, as opposed to Miro2, is the major regulator of mitochondria traffic. Interestingly, cultured hippocampal

[1]Department of Genetics, Yale University School of Medicine, New Haven, CT, USA; [2]Department of Neuroscience, Yale University School of Medicine, New Haven, CT, USA; [3]Department of Cell Biology, Johns Hopkins University School of Medicine, Baltimore, MD, USA; [4]Solomon H. Snyder Department of Neuroscience, Johns Hopkins University School of Medicine, Baltimore, MD, USA.

Correspondence to Marc Hammarlund: marc.hammarlund@yale.edu.

neurons from Miro1 knockout mice still show normal amounts of mitochondria in the axon, although fast axonal mitochondrial transport is dramatically decreased (López-Doménech et al., 2016), suggesting that there are Miro1-independent mechanisms to move mitochondria into the axon in mice, potentially via functional compensation from Miro2, or another unknown adaptor. In addition, a recent study suggests that Miro proteins are not required for TRAK/kinesin-dependent anterograde movement in mouse embryonic fibroblasts (López-Doménech et al., 2018). These conflicting data suggest that our understanding of mitochondria transport in vivo is incomplete.

Studies in *Caenorhabditis elegans* also support the existence of Miro/TRAK-independent mechanisms of mitochondria transport. First, TRAK is not essential for kinesin-1-based transport (Zhao et al., 2021). Second, Miro is not required for axonal mitochondria distribution in some unipolar neurons such as touch receptor neurons and PVQ neurons (Ding et al., 2022; Sure et al., 2018). Third, a recent genetic screen identified the metaxins MTX-1 and MTX-2, components of the mitochondrial sorting and assembly machinery, as important regulators for mitochondria transport (Zhao et al., 2021). In the DA9 neuron, genetic analysis indicated that *mtx-1/2* and *miro-1* redundantly regulate kinesin-1-mediated mitochondria transport and that overexpression of *mtx-1* or *mtx-2* in the PVD neuron can substitute for MIRO-1's function in kinesin-1 based transport but not vice versa (Zhao et al., 2021).

Another protein, RIC-7, is essential for mitochondria localization in *C. elegans*. In *ric-7* mutants, mitochondria are absent from the axons, similar to kinesin-1 mutants (Rawson et al., 2014). RIC-7 does not contain known conserved domains or motifs and does not have an obvious homolog in vertebrates (Rawson et al., 2014). RIC-7 is localized on mitochondria, but how it regulates mitochondria localization in neurons is not understood (Rawson et al., 2014).

Here, we analyze mitochondria transport in vivo using the *C. elegans* AIY and DA9 neurons as model systems. We interrogate the mitochondria transport machinery by tagging the endogenous proteins and visualizing their localization and dynamics in physiological conditions, as well as by genetic analysis using deletion mutants. We find that Miro is important for robust mitochondria anterograde trafficking in axons but is not absolutely required, whereas it is essential for retrograde axonal trafficking. We demonstrate that RIC-7 is specifically required for kinesin-1-based mitochondria trafficking by localizing with kinesin-1 to the leading end of mitochondria. Further, Miro/MIRO-1 and metaxin2/MTX-2 function together to regulate the localization of RIC-7. Using structure/function analysis, we identify the domains in the RIC-7 protein that are crucial for its localization and function. Our work provides new insights into the cellular mechanisms that govern mitochondria traffic in living nematodes and identifies polarized protein localization at the leading end as a novel functional site critical for mitochondria movement.

Results

Axonal mitochondria anterograde transport does not require Miro or TRAK

To assess mitochondria distribution in vivo, we use a matrix-targeted EGFP marker that shows consistent morphology of mitochondria in AIY neurons (see Materials and methods). The AIY neurons are a pair of unipolar interneurons that each extends a single neurite anteriorly, with microtubule plus ends orienting toward the neurite tip (Hill et al., 2019), and have been well established as a model system to study presynaptic assembly and synaptic vesicle localization (Colón-Ramos et al., 2007; Stavoe and Colón-Ramos, 2012; Stavoe et al., 2012; White et al., 1986).

In AIY, partial loss-of-function of *unc-116*, the sole ortholog of *C. elegans* kinesin-1, results in dramatic loss of mitochondria in the neurite (Fig. 1), consistent with an essential role for kinesin-1 in axonal mitochondria anterograde transport (Hurd and Saxton, 1996; Pilling et al., 2006; Rawson et al., 2014). To assess the role of TRAK/Milton and Miro, we used CRISPR to generate deletion alleles of *trak-1*, the sole *C. elegans* TRAK ortholog, and of *miro-1*, -2, and -3, the three *C. elegans* Miro orthologs. We found that mitochondria localization is normal in AIY neurites in *trak-1(KO)* mutants and in a previously published *trak-1 loss-of-function* allele (Zhao et al., 2021) (Fig. 1), consistent with the finding that TRAK-1 is not required for axonal mitochondria anterograde traffic (Zhao et al., 2021). Surprisingly, we found significantly more mitochondria in the AIY neurites of *miro-1(KO)* animals. This is not due to compensation from the other two *miro* genes, as a similar distribution was observed in the *miro-1/2/3* triple knockouts (Fig. 1). The similar phenotypes between the *miro-1* single mutant and the triple mutant indicate that *miro-1* is the major functional ortholog. Further, the different phenotypes of *miro* and *trak* mutants indicate that Miro and TRAK do not have equivalent functions in mitochondria transport, as recent studies have suggested (López-Doménech et al., 2018; Zhao et al., 2021). Overall, these results suggest the existence of Miro- and TRAK-independent mechanisms that are dependent on kinesin-1.

Axonal retrograde transport is blocked in *miro-1* mutants

To exclude the possibility that excessive axonal mitochondria in *miro-1* mutants arise from local biogenesis, we examined overall mitochondria mass during development. We focused on the *miro-1* single mutant since it showed similar mitochondria distribution as *miro-1/2/3* mutants. We used the total fluorescence of our mitochondria marker to estimate relative mitochondria mass and normalized this measurement to that of the control larval stage 1 (L1) animals. Using this assay, we found that there is no significant difference in mitochondria mass between control and *miro-1* mutants at any developmental stage. In both control and *miro-1* mutants, total mitochondria mass increases by ∼40% from L1 to the larval stage 2 (L2) but does not change significantly from L2 to L4 (Fig. 2 A). Next, we examined mitochondria mass specifically in neurites. In control, neurite mass increased dramatically from L1 to L2 (0.12 versus 0.25, P = 0.009) but did not change significantly from L2 to L4 (0.25 versus 0.31, P = 0.79). Strikingly, *miro-1* mutants had a similar amount of neurite mitochondria as L1s but accumulated slightly more as L2s (L1: 0.1, L2: 0.37, P < 0.0001) and dramatically more as L4 (0.77, P < 0.0001 compared with L2) (Fig. 2 B). The increase in neurite mitochondria from L2 to L4 in *miro-1* mutants was accompanied by a corresponding loss of mitochondria in the cell
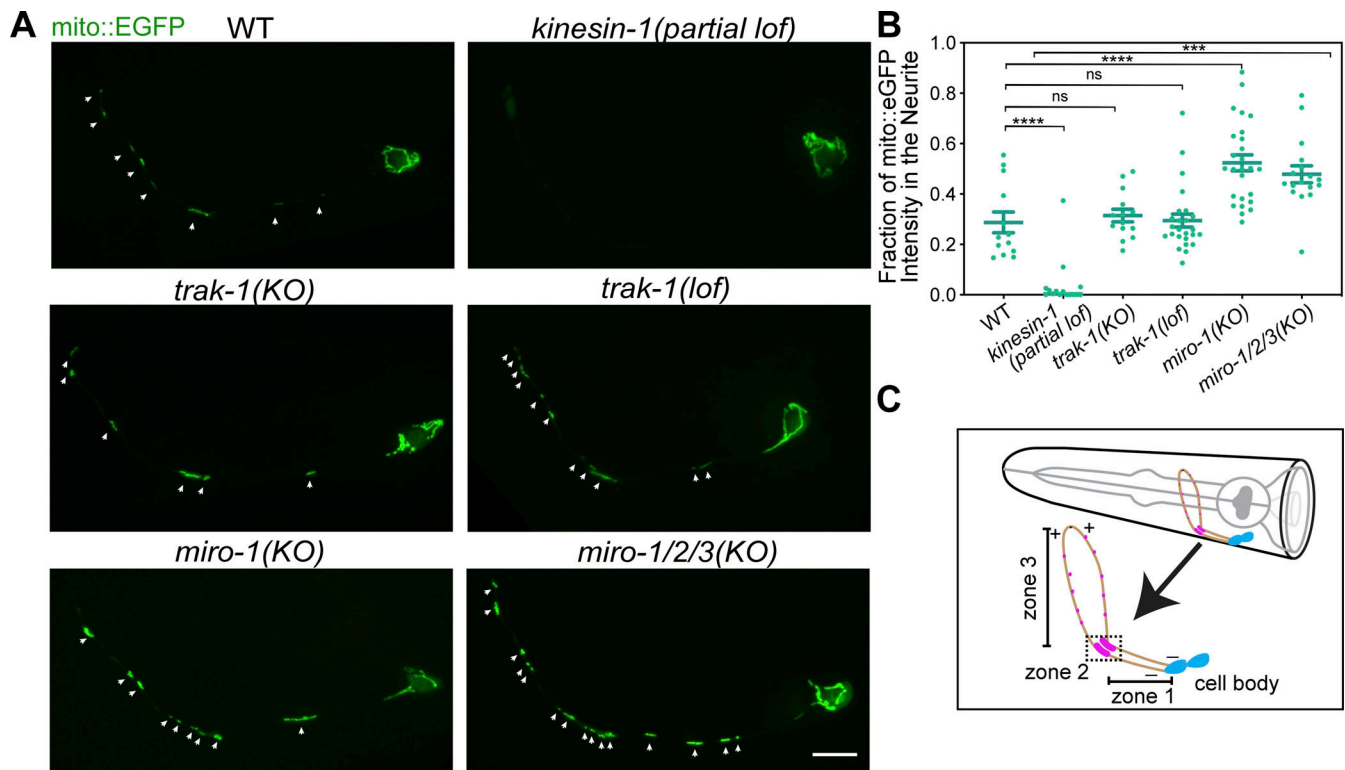
Figure 1. Mitochondria anterograde trafficking requires *kinesin-1/unc-116* and does not depend on *miro* or *trak-1*. (A) Representative images of mitochondria in AIY in WT and different mutant animals. Arrows indicate mitochondria in the axon. Scale bar = 5 μm. **(B)** Quantification of mitochondria in the neurite in WT and different mutant animals. Each data point represents one animal. Data are pooled from five independent experiments, total number of animals: WT = 13, *kinesin-1* = 15, *trak-1*(KO) = 25, *trak-1*(lof) = 14, *miro-1* = 26, and *miro-1/2/3* = 17. Error bars represent SEM. ***P < 0.001, ****P < 0.0001, ns = not significant (one-way ANOVA with multiple comparisons). **(C)** Schematic diagram of the AIY neurons in the *C. elegans* head. The neurite is composed of three zones. Magenta dots in zone 2 and zone 3 indicate the clustering of presynaptic vesicles. Microtubule polarity is indicated by + and −.

body (Fig. 2 C), consistent with the overall stability of mitochondria total mass (Fig. 2 A). Overall, these results suggest that there is an increased net flux of mitochondria in *miro-1* mutants from the cell body into the AIY neurite—in the anterograde direction.

To confirm and extend this result, we used a photoswitchable fluorophore to perform a "pulse-chase" experiment on mitochondria traffic, enabling assessment of mitochondria transport at much longer time scales than is possible by continuous live imaging. This assay is powerful in that it integrates rare or short traffic events over a long period of time. We expressed mitochondria matrix-targeted photoconvertible fluorescent protein Dendra2 and photoconverted mitochondria either in the cell body or in the neurite and imaged after a certain period. Compared with the control animals, mitochondria photoconverted in the cell body showed retarded anterograde traffic to the neurite in *miro-1* mutants. However, after 8 h, the amount of mitochondria that move to the neurite is equivalent to that in controls at 4 h, suggesting that MIRO-1 independent mechanisms are sufficient to move mitochondria into the neurite, albeit less efficiently (Fig. 2, D and F). Consistently, the average gross speed of anterograde trafficking in *miro-1* mutants is reduced by >50%, from 2.9 μm/min to 1.1 μm/s on average (Fig. 2 G; and Videos 1 and 2). By contrast, mitochondria photoconverted in the neurite were retained even after 24 h in *miro-1* mutants, while 80%

were moved back to the cell body in control animals (Fig. 2, E and H). These results indicate that MIRO-1 is essential for mitochondria retrograde movement. Interestingly, although in some cases, Milton/TRAK acts as the adaptor between Miro and dynein (van Spronsen et al., 2013), we found that mitochondria photoconverted in the neurite in *trak-1* mutants were transported back to the cell body, similar to controls, suggesting that TRAK-1 is not required for retrograde movement in AIY unlike Miro (Fig. 2, E and H). Overall, the photoconversion data are consistent with the mitochondria mass experiments and indicate that mitochondria traffic is anterogradely biased in AIY in *miro* mutants, resulting in axonal accumulation and cell body depletion over time.

Together, our results clarify the function of Miro in vivo in *C. elegans*. Miro is important for robust mitochondria movements, both anterograde and retrograde. However, in the absence of Miro, mitochondria transport persists in the anterograde direction, while retrograde transport is completely blocked.

Endogenous RIC-7 localizes at the leading end of mitochondria that undergo anterograde trafficking in the axon

Unlike *miro* mutants, but similar to *kinesin-1* mutants (Fig. 1), *ric-7* mutants lack mitochondria in neuronal processes (Rawson et al., 2014). Consistently, we found that mitochondria are stuck in the AIY cell body in *ric-7* mutants (Fig. 3, A and D). We also
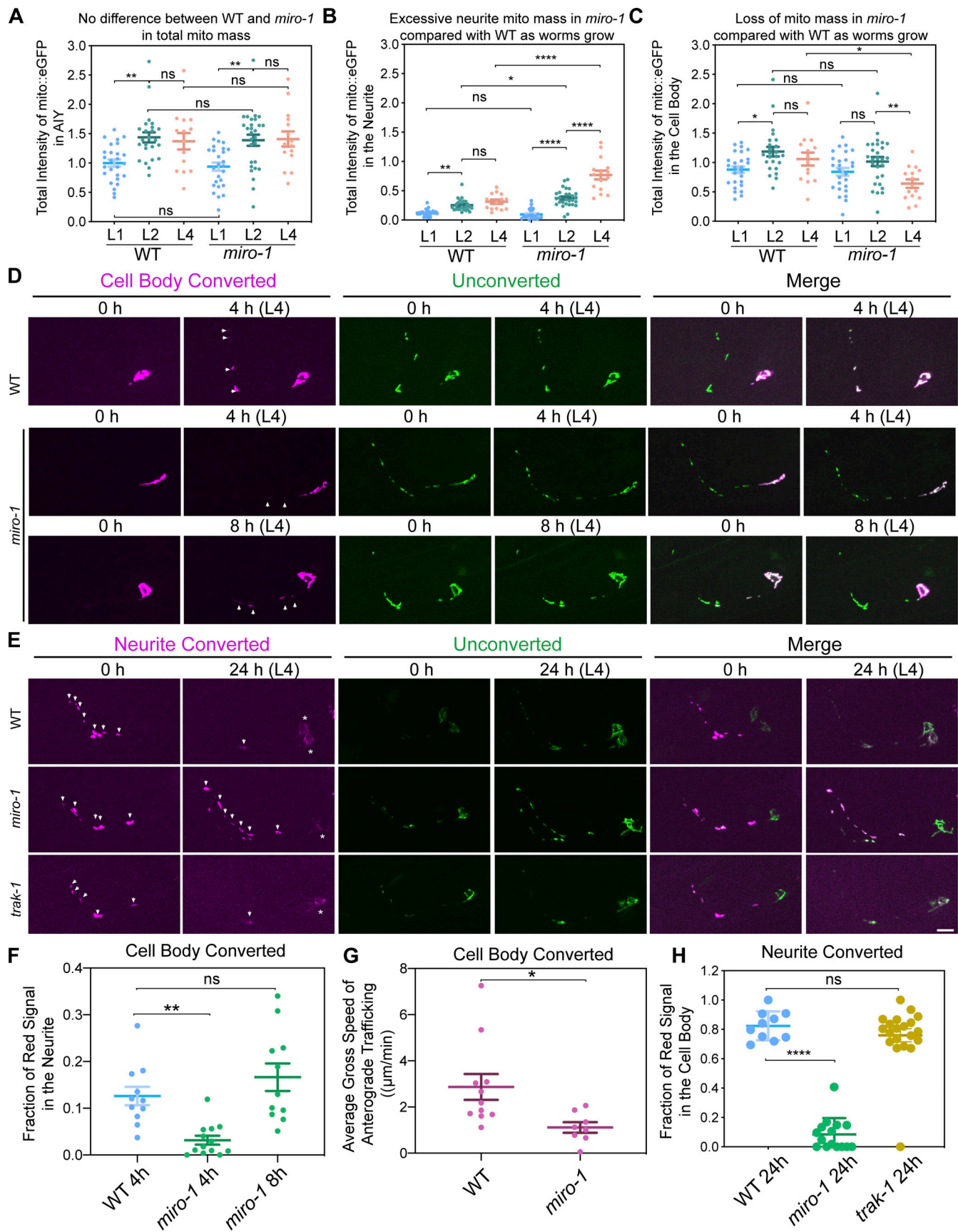
Figure 2. Mitochondria retrograde trafficking requires *miro-1*. (A–C) Quantification of mitochondria mass (indicated by the total intensity of mito:EGFP) in WT and *miro-1* mutant animals at larval stages 1, 2, and 4 (L1, L2, and L4, respectively). Intensity is normalized to that of the whole AIY neuron in WT L1 animals.

performed electron microscopy on wild type and *ric-7* mutants and examined the neuropil, which consists of ~180 axons (Fig. S1 A, "neuropil"). Consistent with fluorescent marker data, we found that in *ric-7* mutants mitochondria are absent from the entire neuropil. In the soma, mitochondria accumulated in *ric-7* animals, but size and morphology were largely unaffected (Fig. S1, A and B), suggesting that *ric-7* is specifically required for mitochondria localization.

Previous studies did not determine whether *ric-7* mutants lack mitochondria specifically in the axon or also in the dendrite.

As microtubule polarity is different in these compartments, and thus the underlying trafficking mechanisms could vary, we sought to test if *ric-7* is required for general mitochondria localization, or if its function is specific to axonal mitochondria. Therefore, we investigated *ric-7*'s role in mitochondria transport in the DA9 neuron, a bipolar excitatory motor neuron with a dendrite in the ventral nerve cord and an axon crossing the body and joining the dorsal nerve cord, where it synapses on the body wall muscle (Fig. 3 C). In DA9, microtubules are plus-end-out in the axon and predominantly minus-end-out in the dendrite (Yan
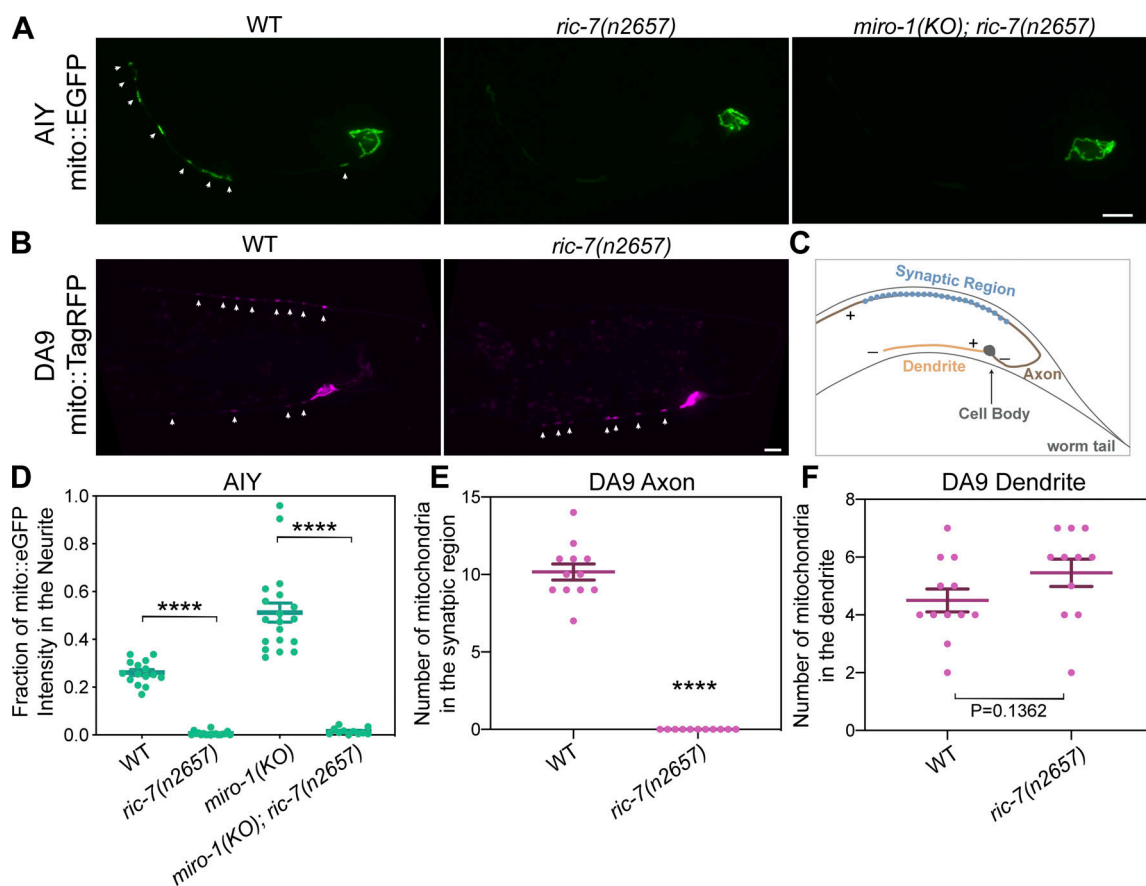
Figure 3. **RIC-7 is required for axonal mitochondria localization. (A)** Representative images of mitochondria in AIY in WT, *ric-7*, and *miro-1; ric-7* mutant animals. Arrows indicate mitochondria. Scale bar = 5 μm. **(B)** Representative images of mitochondria in DA9 in WT and *ric-7* mutant animals. Arrows indicate mitochondria. Scale bar = 5 μm. **(C)** Diagram of DA9 neuron in the worm tail. Only the region shown on the micrographs in B is depicted. Microtubule polarity is indicated by + and −. **(D–F)** Quantification of mitochondria in AIY neurite, DA9 axon, and DA9 dendrite. Each data point represents one animal. Error bars represent SEM. Number of animals for AIY: WT = 15, *ric-7* = 18, *miro-1* = 19, *miro-1; ric-7* = 11. Number of animals for DA9: WT = 12, *ric-7* = 11. ****P < 0.0001 (one-way ANOVA with multiple comparisons for D, two-sided *t* test for E and F).

et al., 2013), and axonal mitochondria anterograde traffic has been shown to depend entirely on kinesin-1, but only partially on MIRO-1 (Zhao et al., 2021).

We found that mitochondria are absent from the DA9 axon in *ric-7* mutants but are still present in the dendrite, indicating that *ric-7* is specifically required to transport mitochondria into axons (Fig. 3, B, E, and F). Consistently, both anterograde and retrograde traffic in the dendrite are not affected in *ric-7* mutants (Fig. S2 A), although the dendritic mitochondria are significantly longer than WT (Fig. S2 B).

We previously observed mitochondria anterograde transport in *miro* mutants in the AIY neurite (Fig. 2 D). Therefore, we tested whether this Miro-independent form of mitochondria traffic is *ric-7* dependent. We found that regardless of the presence or absence of Miro, mitochondria are absent from the AIY neurite in *ric-7* mutants (Fig. 3 D). Thus, anterograde traffic in AIY neurite in the absence of MIRO-1 is also RIC-7 dependent. The AIY neurite and the DA9 axon are similar in that both have plus end-out microtubules, while the DA9 dendrite has predominantly minus end-out microtubules. Together, these results indicate that RIC-7 is specifically essential for the plus end–directed movement of mitochondria—that is, the movement that is mediated by the kinesin-1 motor.

To better understand how RIC-7 regulates mitochondria transport, we used the native and tissue-specific fluorescence (NATF) approach (He et al., 2019) to visualize the endogenous localization of RIC-7 in the DA9 neuron. Briefly, 7xGFP11 was inserted at the endogenous C-terminus of RIC-7 by CRISPR and the complementary GFP1-10 fragment was overexpressed in DA9 (Fig. 4 A). This tagging approach does not affect RIC-7's function as mitochondria localization is not altered (Fig. S3 A). Hereafter, we refer to the endogenous RIC-7 molecules labeled by reconstituted split-GFP as RIC-7::7xSplitGFP. We found that RIC-7::7xSplitGFP formed puncta that are all colocalized with mitochondria (Fig. 4, B–D), although we cannot exclude that some RIC-7 is independent of mitochondria below our detection threshold. By contrast, not every mitochondrion associates with visible RIC-7::7xSplitGFP puncta. We found that the percentage of mitochondria associated with RIC-7::7xSplitGFP is significantly higher in the axon than in the dendrite (80% in axons; 45% in dendrites; P < 0.0001) (Fig. 4 E). Thus, like overexpressed RIC-7 (Rawson et al., 2014), endogenous RIC-7 is highly localized to mitochondria, particularly in the axons.

Since RIC-7 is required for mitochondria localization specifically in the axons (Fig. 3), we speculated that it might be associated with mitochondria that are moving in the anterograde direction in the axon. To test this idea, we performed time-lapse imaging and examined the association of RIC-7 with mobile mitochondria in axons and dendrites. Consistent with previous findings that mitochondria motility is less dynamic in vivo and in mature neurons (Lewis et al., 2016; Smit-Rigter et al., 2016), mitochondria trafficking events are rare in DA9—only ~13% of mitochondria are mobile in the axon during the window of imaging (10 min per video, 10% for anterograde, 3.3% for retrograde, Fig. S3 B). We observed that anterograde mitochondria in the axon (plus-end–directed) invariably (100%, 32/32) associate with RIC-7::7xSplitGFP puncta in contrast to 23% (3/13) of

retrograde mitochondria associated with RIC-7 (Fig. 4 G and Video 4). This localization bias is eliminated in the dendrite (Fig. 4 H). The strict requirement for RIC-7 in mitochondria axonal localization and the strong association of RIC-7 with mitochondria undergoing axonal anterograde movement together suggest that RIC-7 acts on mitochondria to enable their anterograde traffic in the axon.

Interestingly, we observed that the precise localization of RIC-7 on individual mitochondria is sometimes polarized—RIC-7 appears highly localized to one end (Fig. 4, B and C). We found that 28% of all axonal mitochondria have RIC-7 puncta at their distal end, closer to the axon tip. By contrast, only 3% of all axonal mitochondria have RIC-7 puncta at their proximal end, closer to the cell body. This polarized localization pattern is reversed in the dendrite: 0% of all dendritic mitochondria have RIC-7 puncta at their distal end, closer to the dendrite tip, and 25% have RIC-7 puncta at their proximal end (Fig. 4 F). Thus, RIC-7 tends to localize to the mitochondria end that correlates with the direction of the plus end of local microtubules—that is, the leading end for kinesin-1-mediated transport.

We speculated that mitochondria anterograde traffic might be correlated with the polarized localization of RIC-7 at the leading end. We tested this idea using time-lapse imaging. We observed that anterograde trafficking mitochondria in the axon often have RIC-7::7xSplitGFP puncta at their leading end (Fig. 4, I and J; and Videos 3 and 4). However, although we could tell that all anterogradely moving mitochondria are associated with RIC-7 (Fig. 4 G), some mitochondria are too small to allow us to resolve the distribution of RIC-7 on mitochondria. Therefore, to better quantify the relationship between RIC-7's polarized localization and mitochondria traffic, we examined mitochondria exiting the cell body. As previously shown, mitochondria exiting the cell body usually first extend into the neurite, followed by fission and trafficking (Zhao et al., 2021) (Fig. 4 G). Strikingly, as mitochondria extend into the axon, we found that RIC-7 accumulates at the mitochondria tip, leading its way into the axon (Fig. 4, K and L; and Video 5). This happened to all mitochondria we observed entering the axon (8/8, Fig. 4 L). Importantly, we did not observe RIC-7 accumulation at the leading end of mitochondria entering the dendrite (Fig. 4 L and Video 6), indicating that the polarized distribution of RIC-7 is not a pure effect of movement. Overall, these data suggest that RIC-7 acts at the leading end of mitochondria to allow kinesin-1-mediated movement.

Endogenous localization of kinesin-1

As RIC-7 localization is correlated with the directionality of kinesin-1 movement, we labeled endogenous kinesin-1/UNC-116 using the NATF approach (He et al., 2019) and visualized its distribution along with mitochondria in DA9 neurons (Fig. 5, A and B). Although kinesin-1 is known to transport mitochondria, how it is distributed on motile mitochondria has not been reported previously. We found that insertion of 3xGFP11 at the C-terminus doesn't interfere with the function of kinesin-1, as these animals show normal body locomotion, mitochondria localization, and trafficking (Fig. 5, A and B; and Video 7). (We note that 7xGFP11 did interfere with kinesin-1/UNC-116 function;
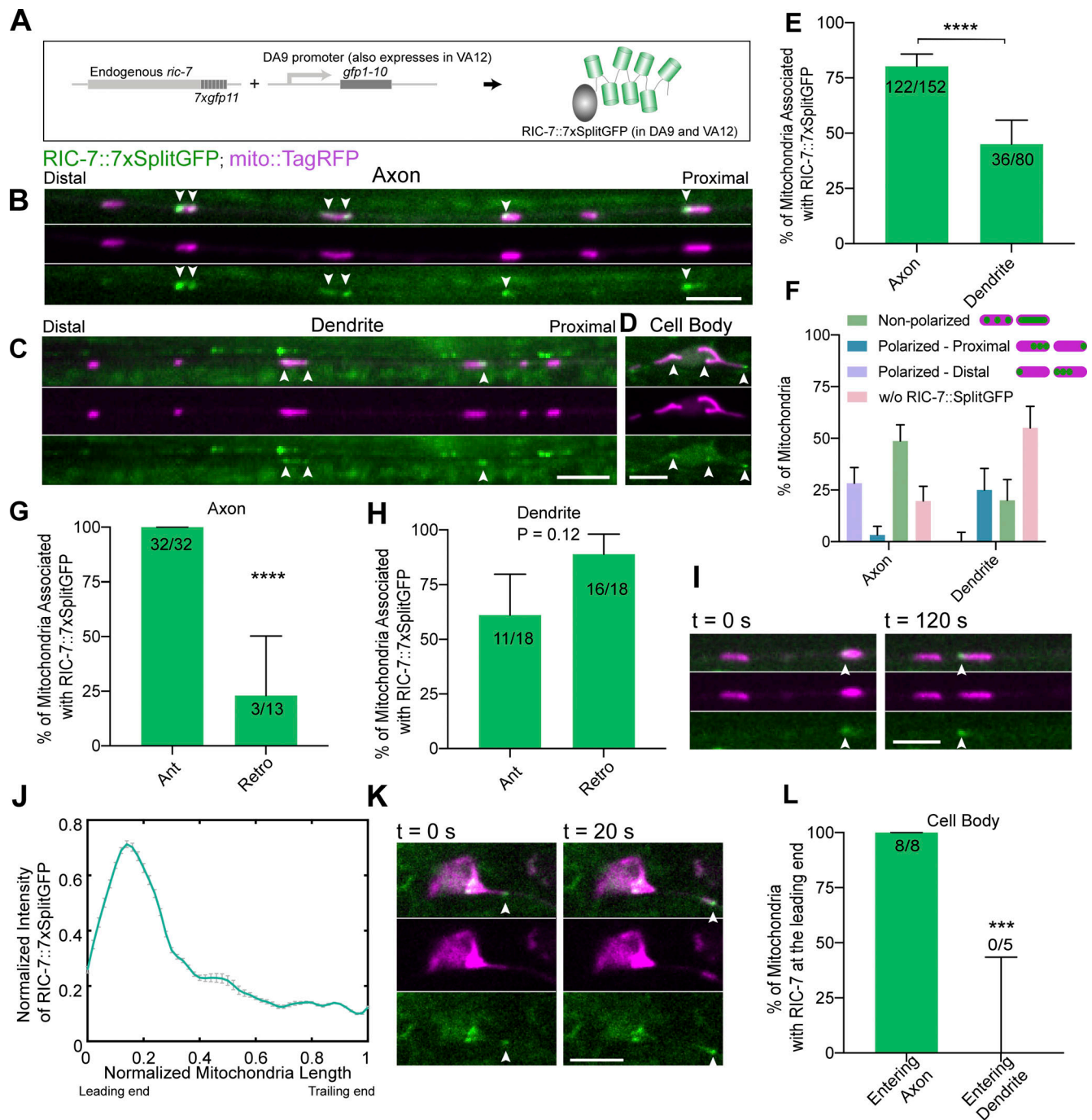
Figure 4. **Endogenous localization of RIC-7. (A)** Labeling scheme of endogenous RIC-7. **(B–D)** Representative images showing RIC-7::7xSplitGFP puncta associated with mitochondria both in the processes and in the cell body. Note that RIC-7 is also labeled with 7xSplitGFP in VA12, the axon of which is visible next to the dendrite of DA9. Arrowheads indicate RIC-7::7xSplitGFP puncta in DA9. Scale bars = 5 μm. **(E)** Percentage of mitochondria associated with RIC-7::7xSplitGFP puncta in the axon and the dendrite was quantified from still images. Number of mitochondria counted are indicated at the top of each bar. Error bars represent 95% confidence intervals. Data are pooled from three independent experiments. Number of animals = 14. ****$P < 0.0001$ (Fisher's exact test). **(F)** Percentage of mitochondria associated with RIC-7::7xSplitGFP based on its polarization status from the same dataset as shown in E. If one or more RIC-7 puncta are localized to the distal or proximal half of the mitochondria, it is regarded as "Distal" or "Proximal." If multiple RIC-7 puncta are spread out on the mitochondria, or if RIC-7 is diffuse and relatively homogenous on the mitochondria, it is regarded as "Non-polarized." Error bars represent 95% confidence intervals. **(G)** Percentage of moving mitochondria associated with RIC-7::7xSplitGFP puncta in the axon. Number of mitochondria counted are indicated at the top of each bar. Error bars represent 95% confidence intervals. Number of animals = 47. ****$P < 0.0001$ (Fisher's exact test). **(H)** Percentage of moving mitochondria associated with RIC-7::7xSplitGFP puncta in the dendrite. Number of mitochondria counted are indicated at the top of each bar. Error bars represent 95% confidence intervals. Data are pooled from 13 independent experiments. Number of animals = 38. P value = 0.12 (Fisher's exact test). **(I)** Representative images of anterogradely trafficking mitochondria in the axon at two different timepoints, with RIC-7::7xSplitGFP accumulating at the leading end, which is indicated by the arrowhead. Scale bar = 2 μm. See Video 4. **(J)** Normalized intensity of RIC-7::7xSplitGFP averaged across different timepoints along the length of mitochondrion shown in Video 4. Leading end is on the left and trailing end on the right. Error bars

represent SEM. **(K)** Representative images of mitochondria entering the axon, with RIC-7::7xSplitGFP accumulating at the leading end, which is indicated by the arrowhead. Scale bar = 5 μm. See Video 5. **(L)** Percentage of mitochondria exiting the cell body with RIC-7::7xSplitGFP accumulation at the tip. Number of mitochondria counted are indicated at the top of each bar. Error bars represent 95% confidence intervals. Data are pooled from five independent experiments. Number of animals = 15. ***P < 0.001 (Fisher's exact test).

we hypothesize that the larger 7× tag may interfere with important interactions.) Endogenous kinesin-1::3xSplitGFP is diffused in the cell body, and throughout the processes, similar to the localization of the endogenous kinesin-1 in *Drosophila* (Kelliher et al., 2018). This diffuse distribution is also consistent with the idea that most kinesin-1 molecules are in the auto-inhibited conformation (Blasius et al., 2007). In addition to this diffuse pool, kinesin-1::3xSplitGFP also forms visible puncta in the cell body and in the axon (Fig. 5 B). Overall, kinesin-1::3xSplitGFP is nearly undetectable in the dendrite, consistent with its plus-end–directed motor activity (Fig. 5, B and C). Live imaging shows that kinesin-1::3xSplitGFP undergoes extensive anterograde and retrograde trafficking in the axon, with no significant directional bias (Fig. 5, D and E). The average speed of anterograde trafficking is 0.97 μm/s, consistent with the reported kinesin-1 velocity measured in vitro (Schnitzer et al., 2000; Verbrugge et al., 2009) (Fig. 5 F). The average speed of retrograde trafficking is 1.78 μm/s. These retrograde events presumably reflect the binding of kinesin-1 to cargoes that are transported back to the cell body by dynein, as it was previously demonstrated that kinesins and dynein can bind to the same cargo in axons (Encalada et al., 2011; Hendricks et al., 2010; Szpankowski et al., 2012). The observed average run lengths of anterograde and retrograde trafficking are 5.2 and 7.8 μm, respectively (Fig. 5 G).

Next, we examined the colocalization of kinesin-1::3xSplitGFP with moving mitochondria. Unlike RIC-7, a substantial fraction of axonal kinesin-1/UNC-116 is not associated with mitochondria. Nevertheless, 80% of axonal anterograde mitochondria (8/10) have visible kinesin-1::3xSplitGFP puncta associated with them. The remaining mitochondria were surrounded by diffuse kinesin-1::3xSplitGFP. Similar to the localization of RIC-7, kinesin-1::3xSplitGFP is enriched at the leading end of anterogradely moving mitochondria, albeit to a lesser extent (Fig. 5, H and I; and Video 7). We suspect that the abundant cytosolic pool of kinesin-1 reduces our ability to assess its fine localization on mitochondria, possibly accounting for the lesser degree of polarized localization. Overall, these experiments provide the first view of kinesin-1's localization on motile mitochondria in vivo and demonstrate that kinesin-1/UNC-116 has polarized localization to the leading end of anterogradely trafficking mitochondria, similar to RIC-7.

Given that kinesin-1 and RIC-7 are both enriched at the leading end of anterograde mitochondria, we sought to examine whether the polarized localization of RIC-7 is dependent on kinesin-1/UNC-116. Mitochondria transport into the axon is blocked in *kinesin-1* mutants, making it impossible to examine RIC-7 localization on axonal mitochondria in this background. Therefore, we performed acute cell-specific knockdown of kinesin-1 using the auxin degron system (Fig. 6 A) (Glomb et al., 2023). After 5 h of auxin treatment, mitochondria in the dendrite accumulate at the distal tip, indicating that kinesin-1 is

degraded and dynein-mediated transport predominates (Fig. 6 B). By contrast, the number of synaptic mitochondria in the axon stayed constant (Fig. 6, B and D). This suggests that in vivo, synaptic mitochondria are anchored by certain mechanisms that allow them to resist transport imbalances, as previously suggested in vitro (Gutnick et al., 2019). We used these synaptic mitochondria to assess the localization of RIC-7 in neurons with reduced kinesin-1. We found that the polarized localization of RIC-7 is nearly abolished after kinesin-1 knockdown (control: 27.3%; auxin: 4.5%; P < 0.0001) (Fig. 6, B, C, and E). We argue that the loss of polarized localization of RIC-7 is not simply a secondary effect caused by the absence of mitochondria anterograde traffic, as the percentage of mobile mitochondria in normal conditions (10% for anterograde, Fig. S3 B) is far less than the percentage of mitochondria with polarized RIC-7 (27–28%, Fig. 4 F and Fig. 6 E). Rather, this result indicates that kinesin-1 is required for polarized RIC-7 localization on mitochondria, likely mediated via its force generation capacity. Further, kinesin-1 knockdown increases the percentage of mitochondria without apparent colocalization of RIC-7 (control: 35.2%; auxin: 57.1%; P = 0.0006) (Fig. 6 E). The decrease in the overall association of mitochondria with RIC-7 might be due to a difference in detection—unpolarized RIC-7 might simply be more difficult to detect. Alternatively, kinesin-1 may help stabilize the localization of RIC-7 on mitochondria. Taken together, these data indicate that kinesin-1 is required for polarized RIC-7 localization on the mitochondria and that RIC-7 binding to mitochondria is largely independent of kinesin-1.

In summary, we find both RIC-7 and kinesin-1 accumulate at the leading end of axonal anterograde mitochondria, and kinesin-1/UNC-116 controls the localization of RIC-7, supporting the hypothesis that kinesin-1 and RIC-7 work together to drive mitochondria movement toward the microtubule plus end.

MIRO-1 and MTX-2 control the localization of RIC-7

Along with MIRO-1, MTX-2 has been identified as an important regulator of mitochondria transport. It is proposed that MTX-2 and MIRO-1 form the adaptor core for both kinesin-1 and dynein motors, with MTX-2 playing the major role (Zhao et al., 2021). Similar to the findings in DA9 and PVD neurons shown in Zhao et al. (2021), the AIY neurite has a reduced number of mitochondria in *mtx-2* mutants and a complete loss of mitochondria in *mtx-2*; *miro-1* double mutants (Fig. 7, A and B). We find that RIC-7 is required for mitochondria transport into axons, but not into dendrites (Fig. 3), in contrast to the Miro-1/metaxin2 combination, which is required for transport into both axons and dendrites (Zhao et al., 2021). Like *ric-7*, EM analysis of *miro-1*; *mtx-2* double mutants shows mitochondria accumulation in the soma (Fig. S1).

To test whether Miro and metaxin2 function independently or together with RIC-7 for kinesin-1-mediated mitochondria
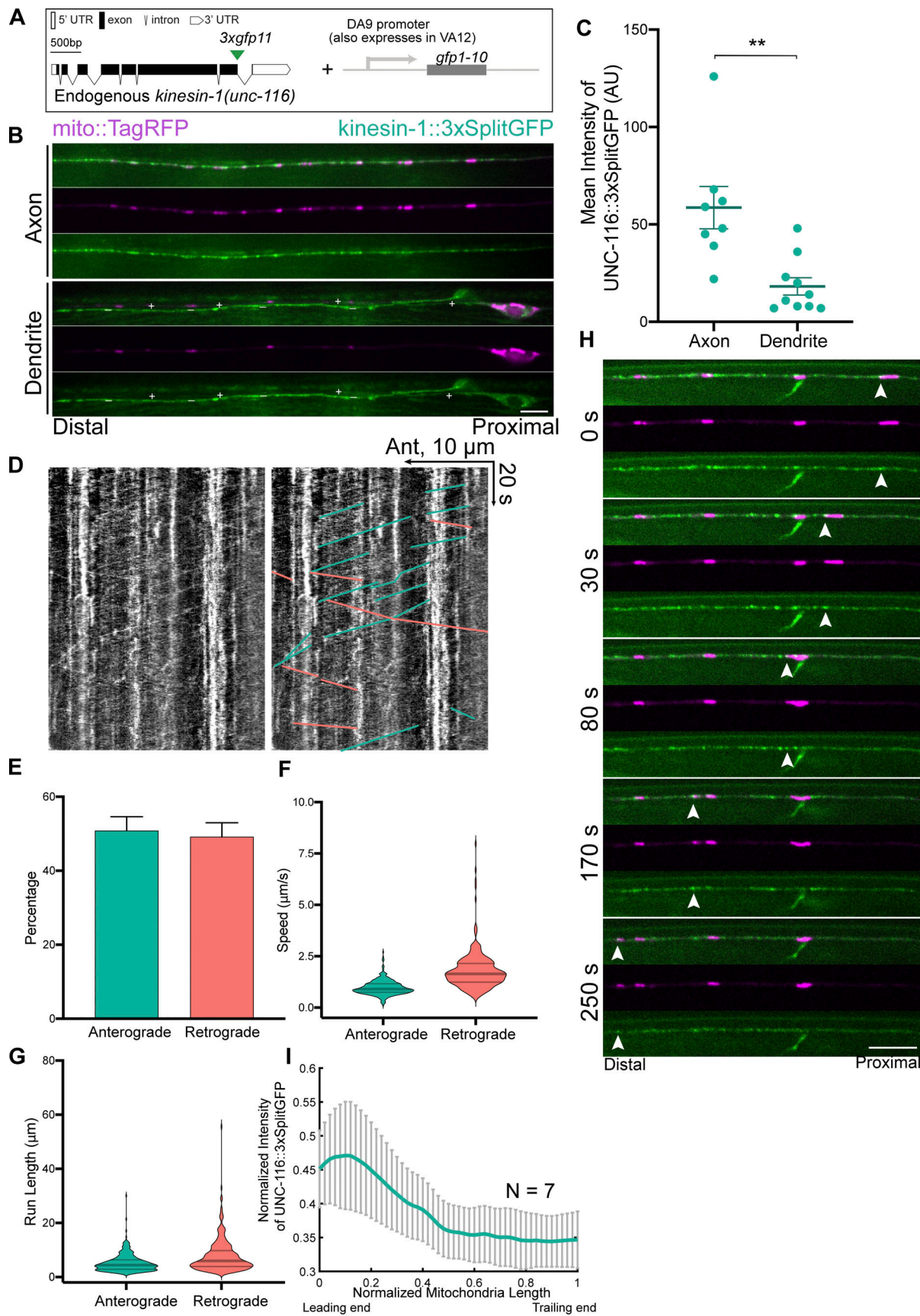
Figure 5. **Endogenous localization of kinesin-1/UNC-116. (A)** Labeling scheme of endogenous kinesin-1/UNC-116. **(B)** Representative images showing the localization of kinesin-1::3xSplitGFP (UNC-116::3xSplitGFP) in the axon and the dendrite. + indicates the DA9 dendrite, whereas — indicates the VA12 axon.

Note that the dendritic kinesin-1::3xSplitGFP is much less abundant. Scale bars = 5 µm. **(C)** Quantification of kinesin-1::3xSplitGFP intensity in DA9 axon and dendrite. Each data point represents one animal. Number of animals: 8 (axon) and 10 (dendrite). **P < 0.01 (*t* test). **(D)** Kymograph showing anterograde and retrograde trafficking events of kinesin-1::3xSplitGFP in the axon with (left) or without (right) manual traces. Green: anterograde; salmon: retrograde. **(E–G)** Quantification of anterograde and retrograde trafficking events of kinesin-1::3xSplitGFP in the axon. **(E)** Percentage of anterograde and retrograde trafficking events, respectively. Error bars represent 95% confidence intervals. **(F and G)** Speeds and run lengths of anterograde and retrograde trafficking events, respectively. Violin plots with median and quartiles are shown. Total number of events analyzed: anterograde = 339; retrograde = 271. Number of animals: 12. **(H)** Representative images showing that kinesin-1::3xSplitGFP is enriched at the leading end of a mitochondrion moving anterogradely. Arrow heads highlight the accumulation of kinesin-1::3xSplitGFP. **(I)** Normalized intensity of kinesin-1::3xSplitGFP along mitochondria length averaged across different timepoints during anterograde trafficking, and then averaged across seven different mitochondria from seven different animals. Leading end is on the left and trailing end on the right. Error bars represent SEM. Data are pooled from four independent experiments.

transport, we characterized RIC-7 localization in *miro-1* and *mtx-2* mutants. In the DA9 cell body of *miro-1* mutants, RIC-7 becomes much more cytosolic and less enriched in mitochondria (Fig. 7 C). We quantified this distribution in two ways, focusing on mitochondria in the cell body since these are present in all genotypes. First, we quantified the enrichment of RIC-7 on

mitochondria by normalizing the intensity of GFP puncta relative to the cytosolic signals (Fig. 7 D, see Materials and methods). Second, we calculated the pixel-by-pixel Pearson's correlation between RIC-7 and mitochondria: the more evenly RIC-7 is distributed, the higher the correlation will be. Using these approaches, we found that RIC-7 is less enriched in mitochondria
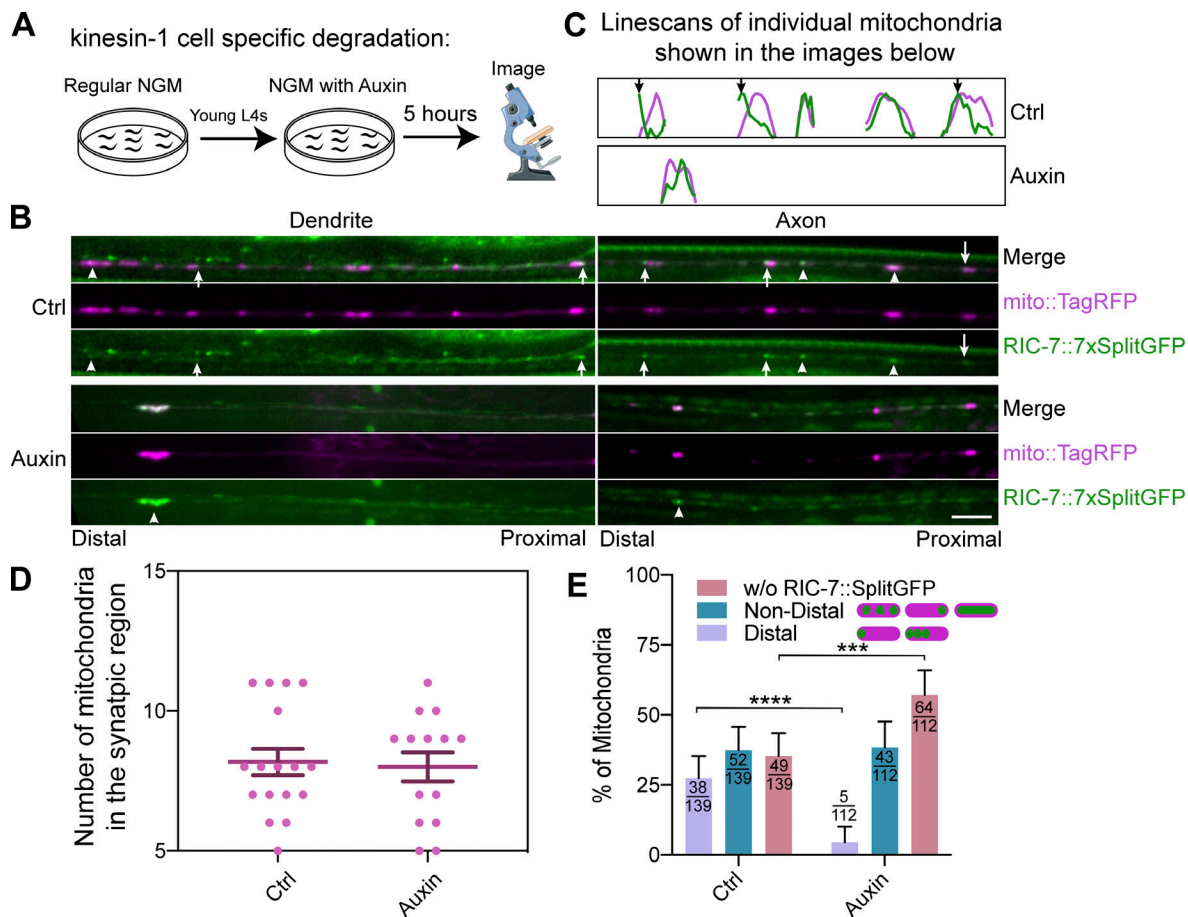
Figure 6. **Kinesin-1 controls the polarized localization of RIC-7. (A)** Schematic representation of cell-specific knockdown of kinesin-1. **(B)** Representative images of control and *kinesin-1/unc-116* knockdown conditions in the dendrite (left) and in the axon (right). Note the accumulation of mitochondria at the distal tip of the dendrite under auxin treatment, indicating kinesin-1 has been efficiently degraded. Arrowheads point to unpolarized RIC-7::7xSplitGFP puncta, while arrows indicate the polarized ones. **(C)** Linescans of individual mitochondria in the axons are shown in B. Green traces represent the intensity of RIC-7:: 7xSplitGFP whereas magenta traces represent that of mito::TagRFP. Arrows indicate the polarized localization of RIC-7::7xSplitGFP. **(D)** The number of axonal mitochondria does not change after 5 h of auxin treatment. Error bars represent SEM. Each data point represents one animal. Data are pooled from three independent experiments. Number of animals: 17 (ctrl) and 14 (auxin). **(E)** Quantification of the percentage of mitochondria based on RIC-7::7xSplitGFP's polarization status. The scoring criteria is the same as Fig. 4 F except that the previous "Non-polarized" and "Proximal" categories are now combined as "Non-distal." Number of mitochondria counted are indicated at the top of each bar. Error bars represent 95% confidence intervals. Same datasets as in D. ***P < 0.001, ****P < 0.0001 (Fisher's exact test).

Wu et al.
Kinesin-1 and RIC-7 lead anterograde mitochondria

Journal of Cell Biology 10 of 20
https://doi.org/10.1083/jcb.202305105
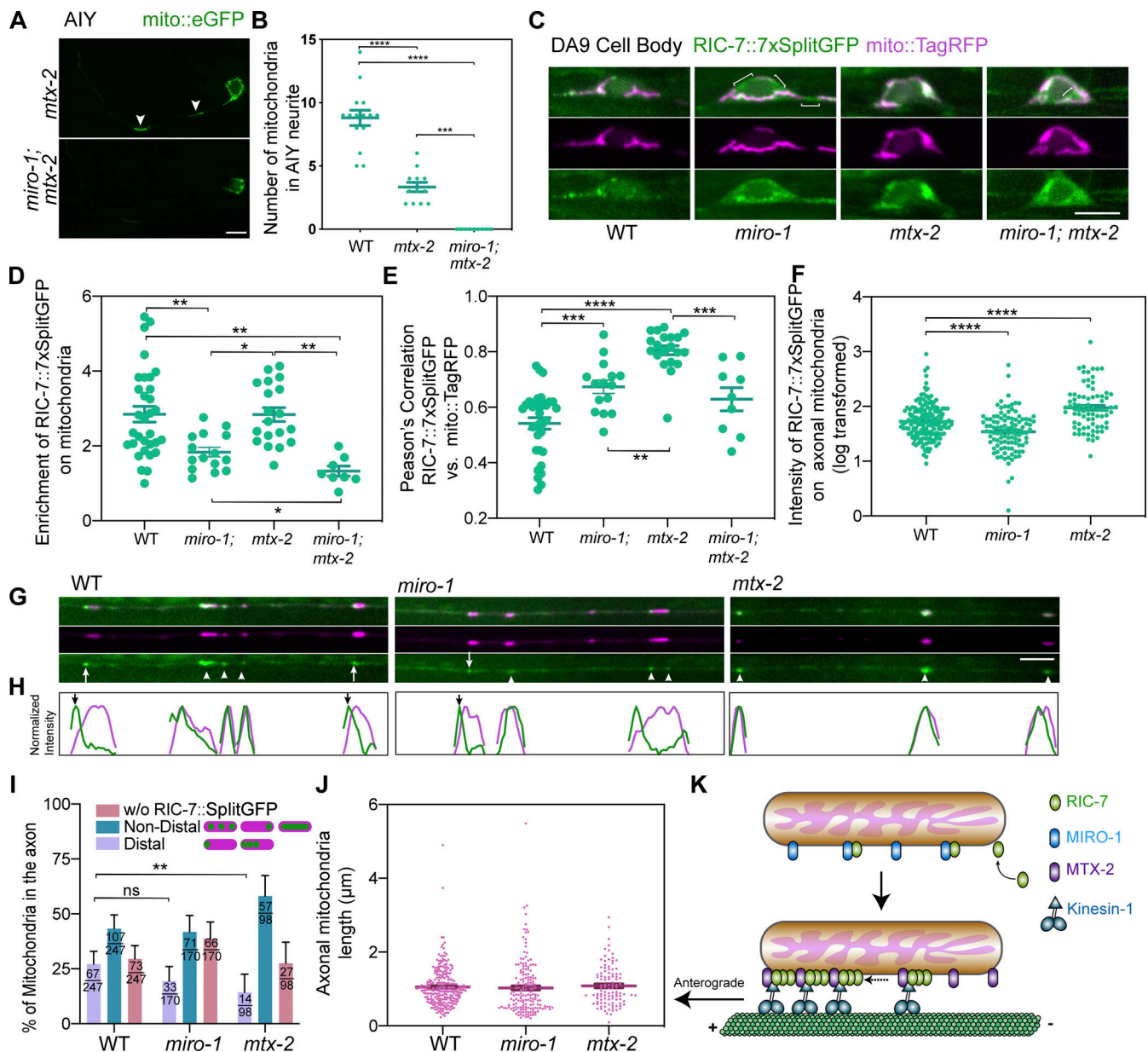
Figure 7. **MIRO-1 and MTX-2 regulate the endogenous localization of RIC-7. (A)** Mitochondria distribution in AIY neurons in *mtx-2* mutant and *mtx-2*; *miro-1* double mutants. Arrowheads indicate mitochondria. Scale bar = 5 µm. **(B)** Quantification of mitochondria in the AIY neurite in WT, *mtx-2* mutant, and *mtx-2*; *miro-1* double mutants. Each data point represents one animal. Data are pooled from two independent experiments, total number of animals: WT = 15, *mtx-2* = 12, *miro-1*; *mtx-2* = 9. Error bars represent SEM. ***P < 0.001, ****P < 0.0001 (one-way ANOVA with multiple comparisons). **(C)** Endogenous RIC-7:: 7xSplitGFP localization in the DA9 cell body of WT, *miro-1*, *mtx-2*, and *miro-1*; *mtx-2* mutants. White brackets in *miro-1*, and *miro-1*; *mtx-2* mutants highlight the increased cytosolic pool of RIC-7::7xSplitGFP. Scale bar = 5 µm. **(D)** Quantification of the enrichment of RIC-7::7xSplitGFP on mitochondria in WT, *miro-1*, *mtx-2*, and *miro-1*; *mtx-2* mutants. Each data point represents one animal. *P < 0.05, **P < 0.01 (one-way ANOVA with multiple comparisons). Data are pooled from four experiments, total number of animals: WT = 33, *miro-1* = 15, *mtx-2* = 20, *miro-1*; *mtx-2* = 8. **(E)** Pearson's correlation between RIC-7::7xSplitGFP and mito:: TagRFP in WT, *miro-1*, *mtx-2*, and *miro-1*; *mtx-2* mutants. Each data point represents one cell body. ***P < 0.001, ****P < 0.0001 (one-way ANOVA with multiple comparisons). Data are pooled from four experiments, total number of animals: WT = 33, *miro-1* = 15, *mtx-2* = 20, *miro-1*; *mtx-2* = 8. **(F)** Mean intensity of RIC-7::7xSplitGFP puncta on axonal mitochondria in WT, *miro-1*, *mtx-2* mutants. The mean intensity of each punctum is presented as log-transformed because the original data is highly skewed and deviated from the normal distribution. One-way ANOVA with multiple comparisons was performed on the transformed data. ****P < 0.0001. Data are pooled from four experiments, total number of animals: WT = 26, *miro-1* = 32, *mtx-2* = 32. **(G)** Endogenous RIC-7:: 7xSplitGFP localization in the DA9 axon of WT, *miro-1*, and *mtx-2* mutants. Arrowheads point to unpolarized RIC-7::7xsplitGFP puncta, while arrows indicate the polarized ones. **(H)** Linescans of individual mitochondria in the axons are shown in F. Green traces represent the intensity of RIC-7::7xSplitGFP whereas magenta traces represent that of mito::TagRFP. To maximize the amplitude of each trace, intensity is normalized in such a way that the maximum intensity is 1 and the lowest value is 0. The arrow indicates the polarized localization of RIC-7::7xSplitGFP. **(I)** Quantification of the percentage of mitochondria based on RIC-7::7xSplitGFP's polarization status. Scoring criteria is the same as Fig. 6 E. The number of mitochondria counted is indicated at the top of each bar. Error bars represent 95% confidence intervals. **P < 0.01, ns = not significant (Fisher's exact test). Data are pooled from four experiments, total number of animals: WT = 26, *miro-1* = 32, *mtx-2* = 32. **(J)** The length of axonal mitochondria in WT, *miro-1*, *mtx-2* mutants. Each data point represents one mitochondrion. Data are pooled

in *miro-1* mutants (1.8-fold) than in WT (2.8-fold, Fig. 7 D), and is significantly more evenly distributed (less punctate) (Fig. 7 E). Consistently, RIC-7 levels on axonal mitochondria are significantly reduced in *miro-1* mutants (Fig. 7 F). Interestingly, RIC-7 is still polarized to the distal end of some axonal mitochondria in *miro-1* mutants (Fig. 7, G–I). These results—together with our functional data (Fig. 2)—indicate that MIRO-1 is important for RIC-7's normal localization and function, but that some of RIC-7's localization and function remain even in the absence of MIRO-1.

In the cell body of *mtx-2* mutants, RIC-7::7xSplitGFP is as enriched on mitochondria as in WT (2.8-fold enrichment). However, unlike in WT where it forms discrete puncta, RIC-7 becomes extremely dispersed over the entire mitochondria, to a greater extent than in *miro-1* mutants (Fig. 7, C and E). In the axon, although RIC-7::7xSplitGFP is still localized to mitochondria, the polarized localization at the leading end is significantly reduced, and this is not due to a change in mitochondria length (Fig. 7, G–J; and Video 8). Thus, MTX-2 has a primary role in enabling RIC-7 localization to mitochondria subdomains. We also noticed a significant increase in RIC-7 levels on axonal mitochondria in *mtx-2* mutants (Fig. 7 F), raising the possibility that MTX-2 might prevent RIC-7 from binding to mitochondria.

In *miro-1*; *mtx-2* double mutants, mitochondria are trapped in the cell body and fail to traffic into both axon and dendrite (Zhao et al., 2021). Thus, the distribution of RIC-7 on axonal mitochondria cannot be determined. In the cell body, combined effects from single mutants were found: RIC-7 does not form discrete puncta and becomes less enriched (1.3-fold) on mitochondria (Fig. 7, C–E).

Overall, this analysis suggests that MIRO-1 and MTX-2 have different roles in mediating RIC-7's localization. MIRO-1 is involved in the overall localization of RIC-7 to mitochondria but some RIC-7 can localize to mitochondria even without MIRO-1. By contrast, MTX-2 is required to enrich RIC-7 at specific loci on mitochondria, functioning together with kinesin-1 to polarize RIC-7 distribution toward the plus-end of microtubules.

Structure/function analysis of RIC-7 identifies regions required for its localization and function

The previous data suggests that RIC-7 has at least two features. First, to localize to mitochondria, partially independently of MIRO-1. Second, to accumulate at the leading end of mitochondria and enable mitochondria anterograde movement. To better understand how RIC-7 functions, we performed a structure/function analysis. The native genomic sequence of the *ric-7* gene spans ~20 kb and overlaps with two other genes, which would make structure/function analysis at the endogenous locus difficult. Therefore, we decided to perform this analysis using transgenes expressed as single-copy insertions at a standardized genomic locus under the same promoter so that different transgenes will achieve comparable levels of expression. The *ric-7* gene encodes for three different splice variants (Fig. S4 B),

two of which (*ric-7a* and *ric-7b*) can rescue mitochondria localization defects in *ric-7* mutants (Rawson et al., 2014). We decided to focus on *ric-7b* because this isoform is preferentially expressed compared with *ric-7a* across different neurons (Fig. S4, B and C) (Taylor et al., 2021).

The predicted structure of RIC-7B by Alphafold (Jumper et al., 2021; Varadi et al., 2022) shows three distinct domains: a relatively ordered domain at the N-terminus (1–99 aa), a largely disordered domain in the middle (100–470 aa), and a structured domain at the C-terminus (471–709 aa) that is similar to the OTU domain in human Otulin, according to HHPred and Dali (Holm et al., 2023; Söding et al., 2005) (Fig. 8 A, Fig. S5 A, and Video 9). The N-terminal and the middle regions do not resemble any known structures. Based on this information, we expressed various deletions of RIC-7 to assess their abilities to restore mitochondria localization in *ric-7* mutants and to visualize their localization by tagging them at the C-terminus with EGFP.

Expression of full-length RIC-7::EGFP restored abundant axonal mitochondria in *ric-7* mutants (Fig. 8 B). Expression of 1–470 aa::EGFP (lacking the region similar to OTU domain) also largely rescued mitochondria localization defects in *ric-7* mutants, suggesting that 471–709 aa is mostly dispensable for RIC-7's function (Fig. 8 B). By contrast, expression of the C-terminal OTU domain 471–709 aa did not restore mitochondria localization in *ric-7* mutants (Fig. 8 B). We also used a stronger pan-neuronal promoter *Prab-3* to drive the expression of either the OTU domain or the human Otulin or OtulinL, none of which could rescue *ric-7* mutants (Fig. S5 B). Consistent with its ability to rescue mitochondria localization in *ric-7* mutants, 1–470 aa::EGFP forms puncta that are colocalized with mitochondria in the axon, some of which are at the distal end, similar to endogenously-tagged RIC-7 (Fig. 8, C–E). We further found that expression of either 1–99 aa or 100–470 aa alone cannot rescue mitochondria localization defects in *ric-7* mutants, indicating that both domains are required for RIC-7's function (Fig. 8 B).

Interestingly, RIC-7 1–99 aa::EGFP colocalizes with mitochondria in both WT and *ric-7* animals (Fig. 8, C and D; and Fig. S4, D–F). In the axon of WT animals, 1–99 aa::EGFP is colocalized with 99% of mitochondria; however, it is only enriched to the distal end of 10% of mitochondria compared with 21% for 1–470 aa::EGFP, suggesting that 100–470 aa helps RIC-7 form puncta at mitochondria subdomains (Fig. 8 E). We surmise that the weak polarized localization of 1–99 aa may be dependent on endogenous RIC-7, but we cannot test this by examining 1–99 aa localization on axonal mitochondria in the *ric-7* mutants as there are no axonal mitochondria. However, consistent with this idea, in the *ric-7* mutants, 1–99 aa::EGFP covers the entire mitochondria in the cell body and the dendrite, unlike the endogenous full-length RIC-7, which forms discrete puncta (Fig. S4, D and E; and Fig. 4, C and D). The pan-mitochondria localization of 1–99 aa::EGFP is not dependent on MIRO-1, suggesting that 1–99 aa
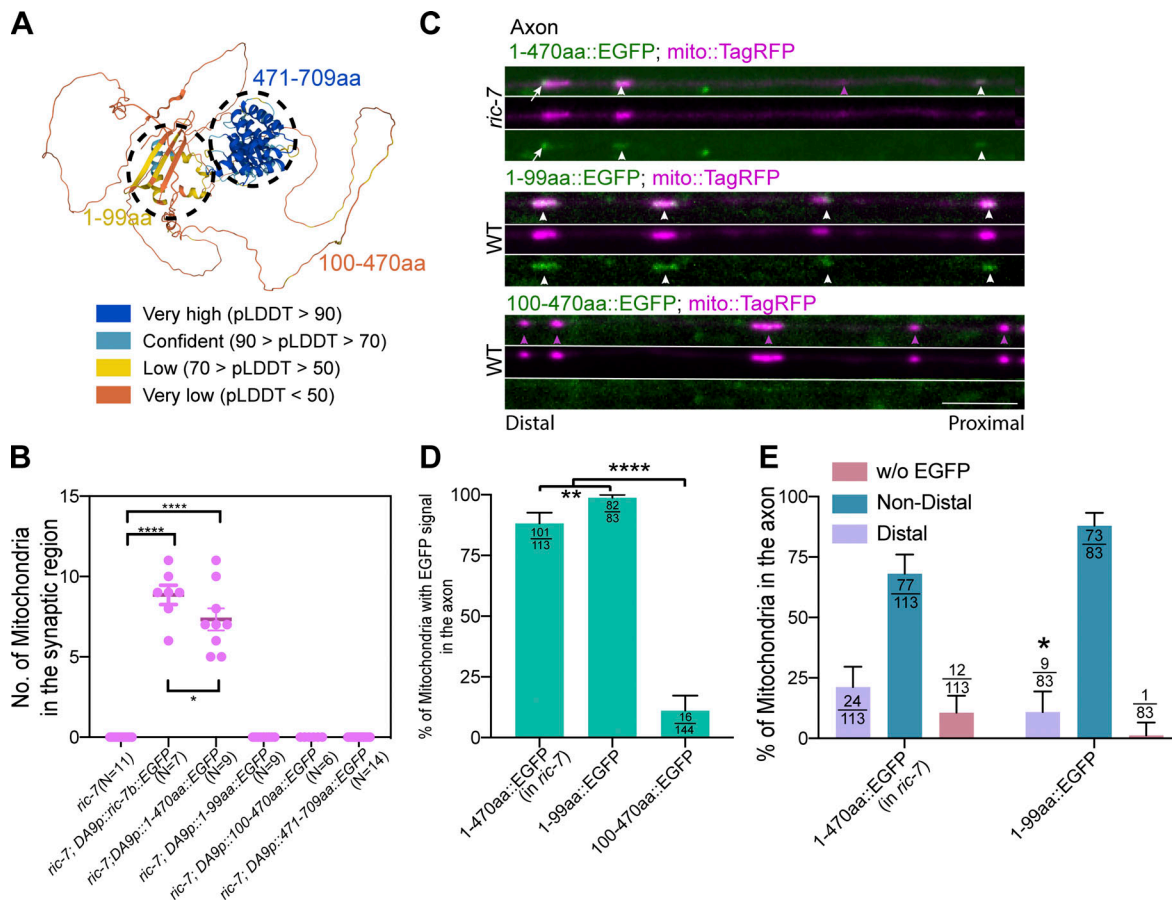
Figure 8. **Structure/function analysis of RIC-7.** (A) 3D structure of RIC-7b predicted by Alphafold. Model confidence is color-coded. The highest confidence region (471–709 aa) is structurally similar to human OTU domain. (B) Quantification of the ability of different RIC-7 truncations to rescue mitochondria localization defects in *ric-7* mutants. Transgenes were driven by *itr-1* promoter (see Materials and methods). Each data point represents one animal. Data are pooled from four experiments. ***P < 0.001, ****P < 0.0001 (one-way ANOVA with multiple comparisons). (C) Localization of truncated proteins. White arrows highlight the distal end localization of 1–470 aa::EGFP; White arrowheads indicate the non-distal localization of truncated proteins; Magenta arrowheads indicate mitochondria that are not associated with the truncated proteins; Scale bar = 5 μm. (D) Quantification of the percentage of mitochondria associated with the GFP transgenic fusions. Number of mitochondria counted are indicated at the top of each bar. Error bars represent 95% confidence intervals. Total number of animals: 1–470 aa = 8; 1–99 aa = 11. **P < 0.01, ****P < 0.0001 (Fisher's exact test). (E) Quantification of the percentage of mitochondria based on the polarization status of the GFP transgenic fusions. Same dataset as in D. *P < 0.05 (Fisher's exact test of Non-distal versus Distal).

contains a mitochondria localization signal that either directly binds to mitochondria or mitochondria protein(s) other than MIRO-1 (Fig. S4 D). By comparison, 100–470 aa::EGFP is largely cytoplasmic in WT animals, with only 11% of axonal mitochondria associated with 100–470 aa::EGFP signals. In *ric-7* mutant animals, this association is slightly increased (49% of dendritic mitochondria contain EGFP signals), suggesting that 100–470 aa can only weakly bind to mitochondria and is displaced by full-length RIC-7 in WT animals (Fig. 8, C and D; and Fig. S4, D–F).

In summary, we find that RIC-7 1–470 aa is sufficient to support mitochondria transport and that 1–99 aa is required for mitochondria localization, while the disordered domain (100–470 aa) facilitates its polarized localization on mitochondria.

Discussion

Mitochondria transport is critical to the maintenance of various neuronal functions. In this study, we used the *C. elegans* AIY neuron and the DA9 neuron as model systems to study

mitochondria transport in vivo. We characterized RIC-7 as an essential regulator of kinesin-1-based mitochondria transport in *C. elegans*. Both kinesin-1 and RIC-7 act at the leading end to drive axonal anterograde mitochondria transport. The N-terminal domain of RIC-7 targets mitochondria, and the disordered domain facilitates RIC-7's accumulation at the mitochondria leading end. We find that a Miro-independent/RIC-7-dependent mechanism can move mitochondria anterogradely, albeit at a much slower rate. RIC-7 partially relies on MIRO-1 to localize to mitochondria and requires MTX-2 to accumulate at the leading end, where RIC-7 promotes kinesin-1-based mitochondria transport (Fig. 7 H). We propose that the polarized localization of kinesin-1 and RIC-7 underlies anterograde mitochondria trafficking in the axon.

RIC-7 functions with Miro and metaxin2 to mediate mitochondria anterograde traffic

Previous studies in multiple model systems showed that the loss of function of Miro results in variable phenotypes in

mitochondria distribution. For example, in *Drosophila* photoreceptors and motor neurons, the loss of function of Miro leads to a dramatic decrease of mitochondria in axons (Guo et al., 2005; Stowers et al., 2002). By contrast, axonal mitochondria distribution was not altered in hippocampal neurons cultured from Miro1 knockout mice, despite the finding that Miro1 is the primary regulator in fast mitochondria trafficking (Guo et al., 2005; López-Doménech et al., 2016; Stowers et al., 2002). In *C. elegans*, loss of Miro does not cause a change in mitochondria number in touch receptor neurons and PVQ neurons (Ding et al., 2022; Sure et al., 2018). By contrast, in the *C. elegans* DA9 neuron, *miro* loss-of-function leads to reduced mitochondria in the axon (Zhao et al., 2021). This study shows that in the AIY neuron, loss of Miro results in increased mitochondria number. What mechanisms might account for these different phenotypes?

We find that in the absence of Miro, mitochondria anterograde transport is retarded. Further, RIC-7 localization to mitochondria is reduced. One possibility is that the right amount of RIC-7 in mitochondria is essential for processive movements, and without MIRO-1, RIC-7 does not reach this optimal level. In this model, all Miro is doing is to localize RIC-7 to mitochondria. Alternatively, Miro itself may promote kinesin-1-mediated mitochondria transport, such as by strengthening the interaction between kinesin-1 and mitochondria. Nevertheless, over long-time scales, mitochondria can still traffic anterogradely in *miro* mutants, in a process that depends entirely on RIC-7 and kinesin-1. Cell type–specific differences in this novel form of Miro-independent mitochondria anterograde traffic may account for the variable phenotype observed in Miro mutants. Alternatively, variation in other mechanisms that affect overall mitochondria distribution, such as dynein-mediated retrograde traffic, actin-mediated short-range movements and/or local anchoring, mitophagy, hitchhiking, etc., might underlie these cell-specific differences (Ashrafi et al., 2014; Basu et al., 2021; Guo et al., 2018; Gutnick et al., 2019; López-Doménech et al., 2018).

Our data also support the idea that metaxin2 is partially redundant with Miro for anterograde mitochondria traffic. We find that loss of *mtx-2* eliminates mitochondria anterograde traffic in Miro mutants in AIY, consistent with previous results in DA9 and PVD (Zhao et al., 2021). Our results also suggest a model in which Miro helps recruit RIC-7 to mitochondria and MTX-2 facilitates the concentration of RIC-7 into puncta on mitochondria. These distinct roles in regulating RIC-7's localization may provide an answer to why MTX-2 can substitute for the function of MIRO-1 in regulating kinesin-1-based movement, but not vice versa (Zhao et al., 2021)—it could be that the enrichment of RIC-7 at the leading end of mitochondria is functionally more important than the overall amount on mitochondria. Together, our data suggest that RIC-7 is a key point of convergence for anterograde traffic and that MTX-2 and MIRO-1 work to coordinate the RIC-7 function.

We also analyzed Miro's role in dynein-based transport. Using photoconversion, we found that mitochondria retrograde trafficking in axons is completely blocked in *miro-1* mutants. Consistently, Miro loss-of-function also results in mitochondria disappearance from DA9 dendrites and PVD anterior dendrites

in *C. elegans* (Zhao et al., 2021). Further, in hippocampal neurons cultured from Miro1 knockout mice, dendritic mitochondria are dramatically reduced while axonal mitochondria distribution is not altered (López-Doménech et al., 2016). Altogether, these results highlight Miro's essential role in dynein-based mitochondria trafficking.

Biochemical and functional analysis suggests that Miro is linked to the dynein/dynactin complex via Milton/TRAK (Brickley and Stephenson, 2011; van Spronsen et al., 2013; Zhao et al., 2021). Surprisingly, we found that mitochondria distribution in the AIY neuron is not altered in *trak-1* mutants, and that retrograde trafficking appears normal. These phenotypes are different from those in DA9 and PVD neurons (Zhao et al., 2021), suggesting that the requirement of Trak for retrograde trafficking is context-dependent. One possibility is that another protein is functionally redundant with Trak to link Miro to the dynein complex in AIY. Alternatively, the *C. elegans* Miro may directly bind to the dynein complex. Indeed, a previous study has shown that human Miro1 can directly bind to kinesin-1 in vitro, without the help of Trak (Macaskill et al., 2009), raising the possibility that the Miro protein may have the capacity to directly bind to motors. These possibilities await further investigation.

Taken together, our data demonstrate that anterograde mitochondria traffic in *C. elegans* relies on two essential factors, kinesin-1 and RIC-7, which function together with Miro and metaxin.

Kinesin-1 and RIC-7 drive mitochondria transport at the leading end

In this study, we found that RIC-7 is specifically required for mitochondria anterograde trafficking in the axon, facilitating kinesin-1-driven mitochondria movements. How does RIC-7 regulate mitochondria transport? One insight comes from its localization pattern. RIC-7 is preferentially enriched at the leading end of anterogradely trafficking mitochondria in the axon. By contrast, MIRO-1 and MTX-2 are ubiquitously distributed in mitochondria (Fu et al., 2020; Zhao et al., 2021). We also found that UNC-116, the sole ortholog of kinesin-1 in *C. elegans*, displays similar mitochondria localization as RIC-7. Previous in vitro studies found that kinesin-1 molecules that are artificially attached to liposomes would dynamically accumulate at the tip of an extending tube. A model was proposed in which lagging kinesin molecules will rapidly move to the growing tip, where they accumulate and exert force on the tube (Leduc et al., 2004). Our data indicate that the dynamic accumulation of kinesin motors on membrane compartments occurs in vivo and that RIC-7 displays similar dynamic localization.

How does RIC-7 facilitate kinesin-1-mediated mitochondria traffic? One model is that RIC-7 is an essential part of the adaptor complex and recruits kinesin-1 to mitochondria. As kinesin-1 accumulates at the leading end due to its motor function, the fluid nature of the mitochondria membrane would allow the adaptor complex to gather at the same spot. Indeed, when linked to kinesin-1 by a light-inducible dimerization system, Miro accumulates at the tip of deformed mitochondria (Song et al., 2022). In this model, the clustering of RIC-7 is a passive consequence of kinesin-1 accumulation at the mitochondria leading

end. Consistent with this model, we found that kinesin-1 degradation leads to the abolishment of the polarized localization of RIC-7 on mitochondria.

However, RIC-7 may also have a specialized function at mitochondria tips. For example, RIC-7 may help stabilize or organize the clustering of kinesin-1/UNC-116. Theoretical analysis has shown that collective force generated by accumulated kinesin-1 motors at the tip allows tube formation (Leduc et al., 2004). In the context of organelle trafficking, the accumulation of motors greatly facilitates organelle movements. For example, an in vivo study has demonstrated that clustering of dynein into microdomains on the membrane of a phagosome facilitates rapid directed transport of the phagosome toward microtubule minus ends. This clustering was proposed to allow cooperative force on a single microtubule (Rai et al., 2016). In vitro, the clustering of small numbers of kinesin-1 by DNA scaffold enables long-distance transport that normally would require high numbers of individual motors (Jiang, 2021). Given the special localization and cellular function of RIC-7, RIC-7 may act as a scaffold to cluster small numbers of kinesin-1 molecules to enable their fast rebinding to microtubules and promote their processivity. Our finding that RIC-7's function requires its disordered sequence may hint at this clustering role, as intrinsically disordered regions are known to contribute to scaffolding function and promote the clustering of other proteins (Cortese et al., 2008).

Potential conservation of RIC-7 outside *C. elegans*

Previous analysis found no obvious mammalian homologs based on the similarity of the primary sequence, and even among nematodes, RIC-7 is highly divergent (Rawson et al., 2014). Using new tools for homology detection (HHPred and Dali), we found that the C-terminus of RIC-7b (471–709 aa) is similar to the human Otulin domain. However, our structure/function analysis showed that this domain is dispensable for RIC-7's function in mitochondria traffic (Fig. 8 B). By contrast, we found that the 1–470 aa fragment of RIC-7 is necessary and sufficient to rescue mitochondria localization defects in *ric-7* mutants. This fragment contains a relatively ordered region (1–99 aa) that can localize to mitochondria and a disordered region (100–470 aa) that is required for RIC-7's function (Fig. 8). The exact molecular function of this disordered region is unclear. Interestingly, unlike 1–470 aa that mimic RIC-7's full-length localization, 1–99 aa are not confined to subdomains of mitochondria (Fig. S4, D and E). This resembles the localization of RIC-7 in *mtx-2* mutants and in kinesin-1 knockdown, suggesting that 100–470 aa may be involved in the interaction between RIC-7 and MTX-2 or kinesin-1. We speculate that potential functional equivalents of RIC-7 in mammalian systems may also be largely composed of a rapidly evolved disordered region, possibly explaining why this critical factor for mitochondria traffic has evaded homology-based searches.

Materials and methods

Worm strains

All strains were maintained at 20°C on NGM plates seeded with OP50 *E. coli*. Strains used in this study are listed in Table S1.

Mitochondria marker selection

In initial attempts to label mitochondria in AIY, we tried three different markers: TOMM-20 transmembrane domain, cytochrome c oxidase subunit 4 (COX-4), and the mitochondria matrix localization signal (MLS) from the chicken mitochondrial aspartate aminotransferase as used in pPD96.32 (Fire Lab Vector Kit). Overexpression of TOMM-20::EGFP exhibited inconsistent mitochondria morphology, sometimes tubular and sometimes globular. Overexpression of COX-4::EGFP resulted in mitochondria fragmentation. In contrast, mitochondria labeled by MLS::EGFP (mito::EGFP in this paper) show consistent tubular morphology. Therefore, we decided to pursue this marker. The microinjection mix contained 30 ng/μl Pttx-3::mito::EGFP::let-858 3′UTR, 30 ng/μl DACR18 (Pttx-3::mcherry::rab-3::unc-10 3′UTR), 25 ng/μ Punc-122::GFP, and Promega 1 kb DNA ladder as the filler. The mix was injected into N2, and transgenic animals with integrated extrachromosomal arrays were then generated by the TMP/UV method. Among several integration lines, we selected *wpIs127* because it expresses the transgenes at a relatively low level and exhibits consistent mitochondria morphology. *wpIs127* was outcrossed five times before further analysis.

Mitochondria in DA9 were labeled by mitochondria matrix localization signal (pPD96.32; Fire Lab Vector Kit) fused with TagRFP and expressed as extrachromosomal arrays. The microinjection mix contained Pitr-1pB::mito::TagRFP::let858 3′UTR at 30 ng/μl, Podr-1::gfp at 20 ng/μl, and Promega 1 kb DNA ladder as the filler.

Molecular cloning

All plasmids used for expressing transgenes in neurons were assembled to the destination vector pCFJ150 using Gateway recombination (Invitrogen). Gibson reactions were used to generate the entry clones (Gibson et al., 2009). Plasmids that express *trak-1* and *miro-1* sgRNAs were made by swapping the N$_{19}$ sequence of the *unc-119* sgRNA from the preexisting plasmid (#46169; Addgene) (Friedland et al., 2013) using PCR, followed by 5′ phosphorylation and blunt end ligation.

All plasmids used in this study are listed in Table S2.

Generation of knock-outs and knock-ins with CRISPR/Cas9

trak-1(wp84), *miro-1(wp88)*, *miro-2(wp92)*, and *miro-3(wp94)* are whole gene deletions generated by NHEJ with CRISPR/Cas9. For *trak-1(wp84)* and *miro-1(wp88)*, CRISPR/Cas9 was performed using the *dpy-10(cn64)* as the co-conversion marker, as previously described in Arribere et al. (2014). Briefly, sgRNA and Cas9 were expressed using plasmids. The microinjection mix contained 50 ng/μl sgRNA vector, 40 ng/μl dpy-10 sgRNA vector, 50 ng/μl Cas9 expression vector (pDD162) (Dickinson et al., 2013), and 26 ng/μl dpy-10 repair template AF-ZF-827 (Arribere et al., 2014). The mix was injected into XE2194, and F1 rollers were genotyped by single-worm PCR. *miro-2(wp92)* and *miro-3(wp94)* were generated by NHEJ using a preassembled Cas9 ribonucleoprotein complex as described in (Dokshin et al., 2018). The injection mix contains 0.25 μg/μl *Streptococcus pyogenes* Cas9 (#1081058; IDT), 0.1 μg/μl tracrRNA (#1072532; IDT), 0.056 μg/μl crRNA in total (0.028 μg/μl for each sequence, synthesized by IDT), and 40 ng/μl PRF4 (rol-6 [su1006]) plasmid.

miro-2 and miro-3 were simultaneously targeted by the same sgRNAs, and the mix was injected into miro-1(wp88) to generate miro triple mutant. F1 progenies (rollers and non-rollers) were screened by single worm PCR.

ric-7::7xgfp11 knock-in was generated by CRISPR/Cas9 using a preassembled Cas9 ribonucleoprotein complex as previously described (Ghanta and Mello, 2020). Briefly, the injection mix contained 0.25 µg/µl S. pyogenes Cas9 (#1081058; IDT), 0.1 µg/µl tracrRNA (#1072532; IDT), 0.056 µg/µl crRNA (synthesized by IDT), 25 ng/µl premelted double-stranded DNA repair template or 0.11 µg/µl of ssDNA repair template and 40 ng/µl PRF4 (rol-6 [su1006]) plasmid. Non-roller F1 progeny from P0 roller jackpot plates were screened by single worm PCR. Homozygotes from the F2 generation were verified by Sanger sequencing.

For unc-116::3xgfp11 and unc-116::AID knock-in, instead of using tracrRNA and crRNA, a single gRNA of 3.7 µg was used (Glomb et al., 2023). This gRNA was synthesized from ssDNA using the EnGen sgRNA Synthesis Kit, S. pygenes (#E3322S; NEB), and subsequently purified using a Monarch RNA cleanup kit (#T2040; NEB).

All repair templates contained ~35 bp homology arms on both ends. For tandem gfp11 insertions, a GSGGGG liker was added between the gene of interest and gfp11. For unc-116, we chose to use 3× tandem repeats instead of 7×, as mitochondria trafficking was dramatically reduced when unc-116 was tagged with 7xgfp11. The repair templates for ric-7::7xgfp11 and unc-116::3xgfp11 were synthesized as a Gblock by IDT, amplified by PCR, gel purified, and further cleaned up with the Qiagen MinElute kit. The repair template for unc-116::AID was synthesized by IDT as ssDNA.

ric-7::7xgfp11 repair template (homology arms, linker, 7xgfp11):

5′-GTCCGGTTCCCCTGTTCTACATACCGGACGATGAAGGAT CCGGAGGTGGCGGGCGTGACCACATGGTCCTTCATGAGTATG TAAATGCTGCTGGGATTACAGGTGGCTCTGGAGGTAGAGATC ATATGGTTCTCCACGAATACGTTAACGCCGCAGGCATCACTG GCGGTAGTGGAGGACGCGACCATATGGTACTACATGAATATG TCAATGCAGCCGGAATAACCGGAGGGTCCGGAGGCCGGGATC ACATGGTGCTGCATGAGTATGTGAACGCGGCGGGTATAACTG GTGGGTCGGGCGGACGAGACCATATGGTGCTTCACGAATACG TAAACGCAGCTGGCATTACTGGCGGATCAGGTGGCAGGGATC ACATGGTACTCCATGAGTACGTGAACGCTGCTGGAATCACAG GCGGTAGCGGCGGTCGGGACCATATGGTCCTGCACGAATATG TCAATGCTGCCGGTATCACCTAATAACTAGGACCCTCTTTTT GTTATTCGTAACTTGTAA-3′

unc-116::3xgfp11 repair template (homology arms, linker, 3xgfp11):

5′-GACAAGTGTATACGTCTCCGTCAGCAGGAATGTCAGGAT CCGGAGGTGGCGGGCGTGACCACATGGTCCTTCATGAGTATG TAAATGCTGCTGGGATTACAGGTGGCTCTGGAGGTAGAGATC ATATGGTTCTCCACGAATACGTTAACGCCGCAGGCATCACAG GCGGTAGCGGCGGTCGGGACCATATGGTCCTGCACGAATATG TCAATGCTGCCGGTATCACCCAAGGAGCTCCAAATGGCTCAA ACGGTGTGTTTAG-3′

unc-116::AID repair template (Glomb et al., 2023, homology arms, AID):

5′-GACAAGTGTATACGTCTCCGTCAGCAGGAATGTCAATGC CTAAAGATCCAGCCAAACCTCCGGCCAAGGCACAAGTTGTGG GATGGCCACCGGTGAGATCATACCGGAAGAACGTGATGGTTT CCTGCCAAAAATCAAGCGGTGGCCCGGAGGCGGCGGCGTTCG TGAAGCAAGGAGCTCCAAATGGCTCAAACGGTGTGTTTAG-3′

All gRNA sequences used in this study are listed in Table S3. Primers used for genotyping are listed in Table S4. Allele sequences are listed in Table S5.

Structure/function analysis of RIC-7

Structure/function analysis of RIC-7 was performed by expressing different transgenes as single-copy insertions at the same genomic locus under the same promoter to achieve comparable levels of expression. As the endogenous expression level of RIC-7 in DA9 is extremely low (Fig. S4 A) (Taylor et al., 2021), we initially used a weak promoter, Pitr-1pB, to drive the expression of transgenes in DA9 (Klassen and Shen, 2007; Taylor et al., 2021). Using this approach, mitochondria localization is restored when ric-7b full length is expressed, suggesting that the expression level is high enough for the functional assessment of the truncated proteins. However, it is not high enough for us to reliably examine the localization of the proteins. Therefore, we switched to a stronger DA9 promoter, Pmig-13 (Klassen and Shen, 2007) (Fig. S4 A), to examine protein localization.

CRISPR/Cas9 was used to generate single-copy insertion at the ttTi5605 landing site on Chromosome I in the strain EG8078. The injection mix contained 0.25 µg/µl S. pyogenes Cas9 (#1081058; IDT), 0.1 µg/µl tracrRNA (#1072532; IDT), 0.028 µg/µl crRNA each (synthesized by IDT), the transgene plasmid constructed in pCFJ150 (100 ng/µl), pMA122 (peel-1 negative selection, 10 ng/µl), and pCFJ90 (Pmyo2::mCherry, 1.5 ng/µl). Each injected P0 animal was singled and grown for 7–8 days at room temperature until starvation followed by heat shock at 34°C for 4 h. The next day after heat shock, P0 plates were checked for potential insertions. Successful insertions should survive the heat shock, not express mCherry, and be non-unc. ~10 non-unc worms from each P0 plate were singled and verified for insertion by genotyping.

Auxin-induced single-cell specific knock down of kinesin-1/unc-116

To acutely knock down kinesin-1/unc-116 in DA9 (Glomb et al., 2023), young L4 animals were cultured on NGM plates containing 1 mM Auxin (#A10556.14; Thermo Fisher Scientific) for 5 h before imaging. Animals of the same stage cultured on NGM plates lacking auxin served as controls.

Fluorescence microscopy

To visualize mitochondria distribution in AIY and DA9, L4 animals were immobilized by 8 mM levamisole and mounted on 3% agarose pad. Still images were acquired with an ORCA-Flash4.0 camera (Hamamatsu) on a VT-iSIM system (BioVision) built around a Leica Laser Safe DMi8 Inverted scope with a PL APO 100×/1.47 OIL CORR TIRF objective for AIY or a HC PL APO 63×/1.40 OIL CS2 objective for DA9. Image acquisition was controlled by MetaMorph Advanced Confocal Acquisition Software Package. The AIY neuron that is closer to the coverslip was imaged. Z-stacks were acquired with a step size of 0.2 µm to capture the whole neuron.

Wu et al.
Kinesin-1 and RIC-7 lead anterograde mitochondria

Journal of Cell Biology
https://doi.org/10.1083/jcb.202305105

16 of 20

To better image the endogenous proteins and mitochondria in DA9, L4 animals were immobilized with 50 mM Muscimol for 2–3 min before mounting, which increases the chance that either the dorsal or the ventral side faces the coverslip. Images were acquired with a HC PL APO 63×/1.40 OIL CS2 objective. Emission filters 525/50 and 605/52 nm were used for 488 and 561 nm illumination, respectively. Images were taken at 400 ms exposure sequentially for 488 and 561 nm at each Z position. Only the dendrite or the axon was imaged for each animal depending on the orientation. Time-lapse imaging was performed for 10 min with 10-s intervals, with three z-steps of 0.2-μm step size.

To generate the kymograph of kinesin-1::3xSplitGFP (UNC-116::3xSplitGFP) trafficking, images were taken continuously on a single plane at 400 ms exposure with the 488-nm laser using the streaming mode.

For Photoconversion in the AIY neuron, images were acquired on a UltraVIEW VoX spinning-disc confocal microscope (PerkinElmer) built around a Nikon Ti-E Eclipse equipped with a 60×/1.4NA CFI Plan Apo objective and a Hamamatsu C9100-50 camera and driven by the Velocity software (Improvision). Mitochondria in the cell body or the axon in both AIY neurons were photoconverted with a 405 nm laser using the PhotoKinesis Unit. After photoconversion, worms were recovered and placed on NGM plates with OP50. After a certain period (4, 8, or 24 h), these worms were imaged again. All animals were staged to be photoconverted so that the endpoint was at L4. For time-lapse imaging, young L4 animals were immobilized by 8 mM levamisole for 5 min and then washed with M9 at least five times before mounting on a 10% agarose pad, which is in turn mounted on a gas permeable slide to minimize hypoxia. Videos were taken with 0.3 μm z-step size at 1–2 min intervals for WT for a total duration of 1–2 h and 5-min intervals for *miro-1* mutants for 4–6 h. We were not able to assess the detailed characteristics of mitochondria transport in *miro-1* mutants as this requires shortening the imaging interval, and we found that mitochondria trafficking in *miro-1* mutants was very sensitive to laser exposure.

All fluorescent images were acquired at room temperature (~22°C).

Image analysis for fluorescence microscopy
To quantify mitochondria in the AIY axon, we used two different metrics: (1) the fraction of the total fluorescence of mito::EGFP in the axon; (2) the number of mitochondria in the axon. We arrived at the same conclusion using both metrics. The first metric is defined by the following formula: the total intensity of the axon/(the total intensity of the cell body + the axon), which was calculated with a custom Matlab script, using maximum projection images. Briefly, images were imported to Matlab using the function "imread." After background subtraction, images were threshold-segmented using the functions "adaptthresh" and "imbinarize." The total intensity of the cell body and the axon were then calculated in Matlab by integrating each pixel under the segmented images, respectively. To quantify mitochondria in DA9 axon, only the second metric was used.

To quantify the enrichment of RIC-7::7xSplitGFP and kinesin-1::3xSplitGFP (UNC-116::3xSplitGFP) at the leading end of anterogradely trafficking mitochondria, line scans of the GFP fluorescence intensity along the length of mitochondria were generated in FIJI. After background (intensities outside of the neuron but inside the worm) subtraction, the intensity values were averaged across different timepoints over the course of the movements, including the period when mitochondria were paused, and then normalized to the maximum value of all time points. To average across different mitochondria that differ in length (Fig. 5 I), the values at 51 regularly spaced points along the mitochondria length were estimated using linear interpolation with the interp1 function in Matlab.

Kymographs of kinesin-1::3xSplitGFP (UNC-116::3xSplitGFP) trafficking were generated and analyzed using KymoToolBox.

To compare RIC-7 localization in different genotypes, two different methods were used: (1) enrichment on mitochondria (Fig. 7 D); (2) Pearson's correlation (Fig. 7 E). Enrichment on mitochondria is defined as the ratio between the intensity of RIC-7::7xSplitGFP puncta on mitochondria and the cytosolic GFP signals, both of which were manually measured in ImageJ and background subtracted. For *mtx-2* and *miro-1*; *mtx-2* double mutants where RIC-7::7xSplitGFP does not form discrete puncta, the GFP intensity on the entire mitochondria was measured. For Pearson's correlation, the DA9 cell body excluding the nucleus was manually specified in ImageJ, and then a customized macro in ImageJ was used to get the intensities of each pixel in both channels. Pearson's Correlation between RIC-7::7xSplitGFP and mito::TagRFP was calculated using the Matlab function corrcoef.

Electron microscopy and analysis
For ultrastructural analysis of N2, *ric-7*, *miro-1*; *mtx-2*, and *unc-116* mutants, we subjected young adult worms to high-pressure freezing (EM ICE, Leica Microsystems). Type-A (3-mm diameter; Technotrade) specimen carriers were immersed in Hexadecane and blotted on a piece of filter paper so that the sides of carriers specimens mounted were coated with a thin layer of Hexadecane. This coating allows easy removal of specimens from carriers after processing. The 100-μm side of a Type-A specimen carrier was first filled with OP50 to the rim of the carrier. Using a worm pick, ~10 adult animals were placed on top of OP50. A flat side of a Type-B specimen carrier (3-mm diameter; Technotrade) was immersed in Hexadecane and placed on top of the Type-A carrier without blotting such that residual Hexadecane would fill any remaining space between animals and the Type-B carrier. This process would ensure no air bubbles were trapped inside the specimen carrier sandwich. Once assembled, the specimen carrier was loaded into a high-pressure freezer and frozen immediately. Specimens were kept under liquid nitrogen until further processing.

Once all samples were frozen, they were transferred into freeze-substitution media containing 1% osmium tetroxide, 1% glutaraldehyde, 1% water, and anhydrous acetone, which was precooled in an automated freeze substitution unit (AFS 2, Leica Microsystems) to –90°C. The freeze-substitution was carried out with the following protocol: –90°C for 48 h, 5°C/h to –20°C, –20°C for 12 h, and 10°C/h to 20°C. Once completed, specimens were infiltrated into plastic (Epon-Araldite, TedPella, Epon, 6.2 g; Araldite, 4.4 g; DDSA, 12.2 g; and BDMA 0.8 ml) over ~20 h

Wu et al.
Kinesin-1 and RIC-7 lead anterograde mitochondria

Journal of Cell Biology 17 of 20
https://doi.org/10.1083/jcb.202305105

(30% Epon-Araldite/acetone for 3 h, 70 % for 4 h, 90 % overnight). On the next day, specimens were embedded into 100% Epon-Araldite and cured for 48 h. 70-nm serial sections were prepared using an ultramicrotome (UC7, Leica Microsystem) and collected onto Pioloform (EMS)-coated grids (single slot, Ted Pella). Roughly 200 sections were collected from each specimen around the head ganglia region. After staining with 2.5% uranyl acetate, sections were imaged on a transmission electron microscope (Talos L120C; Thermo Fisher Scientific) equipped with Ceta Camera (Thermo Fisher Scientific). The number of mitochondria and diameter of each mitochondrion were measured blind to genotypes using Fiji. The data are plotted in Prism (GraphPad, v10).

Statistical analysis

All statistical analysis was performed in GraphPad Prism. Two-sided Fisher's exact tests were used for binary data. For non-binary data, unless otherwise noted, two-sided t test was used to compare two groups, and one-way ANOVA test followed by Dunn's multiple comparisons test was used to compare multiple groups. Data distributions were assumed to be normal, but this was not formally tested.

Online supplemental material

Fig. S1 shows the electron microscopy data of the soma and/or neuropil area in WT, *ric-7*, *miro-1*; *mtx-2*, and kinesin-1 mutants. Fig. S2 shows the quantification of mitochondria trafficking events in the DA9 dendrite in WT and *ric-7* mutant. Fig. S3 shows the mitochondria distribution and the percentage of mobile mitochondria in the DA9 axon in the strain where RIC-7 is endogenously tagged with 7xSplitGFP. Fig. S4 shows extended data of the structure/function analysis of RIC-7. Fig. S5 shows that human Otulin or OtulinL or the C-term domain of RIC-7 cannot rescue mitochondria localization in *ric-7* mutant. Videos 1 and 2 show mitochondria trafficking in the AIY neuron in WT and *miro-1* animals, respectively. Videos 3, 4, 5, and 6 show mitochondria trafficking in different places in the DA9 neuron in the strain where RIC-7 is tagged with 7xSplitGFP (S3: an axon segment close to the cell body; S4: in the synaptic region in the DA9 axon; S5: cell body and the proximal axon; and S6: cell body and the proximal dendrite). Video 7 shows mitochondria trafficking in the DA9 neuron in the strain where kinesin-1 is endogenously tagged with 3xSplitGFP. Video 8 shows mitochondria trafficking in the DA9 neuron in the *mtx-2* mutant where RIC-7 is endogenously tagged with 7xSplitGFP. Video 9 shows the 3D structure comparison between RIC-7b and Otulin prepared by Dali. Tables S1, S2, S3, S4, and S5 list the strains, plasmids, gRNA sequences, primers, and allele sequences used in this study, respectively.

Data availability

All data are available in the main text or the supplementary materials.

Acknowledgments

We would like to thank members of the Hammarlund Lab and Yogev Lab for technical support and discussion, Dr. Shawn

References

Amiri, M., and P.J. Hollenbeck. 2008. Mitochondrial biogenesis in the axons of vertebrate peripheral neurons. *Dev. Neurobiol.* 68:1348–1361. https://doi.org/10.1002/dneu.20668

Arribere, J.A., R.T. Bell, B.X. Fu, K.L. Artiles, P.S. Hartman, and A.Z. Fire. 2014. Efficient marker-free recovery of custom genetic modifications with CRISPR/Cas9 in *Caenorhabditis elegans*. *Genetics*. 198:837–846. https://doi.org/10.1534/genetics.114.169730

Ashrafi, G., J.S. Schlehe, M.J. LaVoie, and T.L. Schwarz. 2014. Mitophagy of damaged mitochondria occurs locally in distal neuronal axons and requires PINK1 and Parkin. *J. Cell Biol.* 206:655–670. https://doi.org/10.1083/jcb.201401070

Baldwin, K.R., V.K. Godena, V.L. Hewitt, and A.J. Whitworth. 2016. Axonal transport defects are a common phenotype in *Drosophila* models of ALS. *Hum. Mol. Genet.* 25:2378–2392.

Basu, H., G. Pekkurnaz, J. Falk, W. Wei, M. Chin, J. Steen, and T.L. Schwarz. 2021. FHL2 anchors mitochondria to actin and adapts mitochondrial dynamics to glucose supply. *J. Cell Biol.* 220:e201912077. https://doi.org/10.1083/jcb.201912077

Blasius, T.L., D. Cai, G.T. Jih, C.P. Toret, and K.J. Verhey. 2007. Two binding partners cooperate to activate the molecular motor Kinesin-1. *J. Cell Biol.* 176:11–17. https://doi.org/10.1083/jcb.200605099

Brickley, K., and F.A. Stephenson. 2011. Trafficking kinesin protein (TRAK)-mediated transport of mitochondria in axons of hippocampal neurons. *J. Biol. Chem.* 286:18079–18092. https://doi.org/10.1074/jbc.M111.236018

Colón-Ramos, D.A., M.A. Margeta, and K. Shen. 2007. Glia promote local synaptogenesis through UNC-6 (netrin) signaling in *C. elegans*. *Science*. 318:103–106. https://doi.org/10.1126/science.1143762

Cortese, M.S., V.N. Uversky, and A.K. Dunker. 2008. Intrinsic disorder in scaffold proteins: Getting more from less. *Prog. Biophys. Mol. Biol.* 98: 85–106. https://doi.org/10.1016/j.pbiomolbio.2008.05.007

Davis, A.F., and D.A. Clayton. 1996. In situ localization of mitochondrial DNA replication in intact mammalian cells. *J. Cell Biol.* 135:883–893. https://doi.org/10.1083/jcb.135.4.883

De Vos, K.J., A.L. Chapman, M.E. Tennant, C. Manser, E.L. Tudor, K.F. Lau, J. Brownlees, S. Ackerley, P.J. Shaw, D.M. McLoughlin, et al. 2007. Familial amyotrophic lateral sclerosis-linked SOD1 mutants perturb fast axonal transport to reduce axonal mitochondria content. *Hum. Mol. Genet.* 16:2720–2728. https://doi.org/10.1093/hmg/ddm226

Dickinson, D.J., J.D. Ward, D.J. Reiner, and B. Goldstein. 2013. Engineering the *Caenorhabditis elegans* genome using Cas9-triggered homologous recombination. *Nat. Methods.* 10:1028–1034. https://doi.org/10.1038/nmeth.2641

Ding, C., Y. Wu, H. Dabas, and M. Hammarlund. 2022. Activation of the CaMKII-Sarm1-ASK1-p38 MAP kinase pathway protects against axon degeneration caused by loss of mitochondria. *Elife*. 11:e73557. https://doi.org/10.7554/eLife.73557

Dokshin, G.A., K.S. Ghanta, K.M. Piscopo, and C.C. Mello. 2018. Robust genome editing with short single-stranded and long, partially single-stranded DNA donors in *Caenorhabditis elegans*. *Genetics*. 210:781–787. https://doi.org/10.1534/genetics.118.301532

Encalada, S.E., L. Szpankowski, C.H. Xia, and L.S. Goldstein. 2011. Stable kinesin and dynein assemblies drive the axonal transport of mammalian prion protein vesicles. *Cell*. 144:551–565. https://doi.org/10.1016/j.cell.2011.01.021

Fransson, A., A. Ruusala, and P. Aspenström. 2003. Atypical Rho GTPases have roles in mitochondrial homeostasis and apoptosis. *J. Biol. Chem.* 278:6495–6502. https://doi.org/10.1074/jbc.M208609200

Friedland, A.E., Y.B. Tzur, K.M. Esvelt, M.P. Colaiácovo, G.M. Church, and J.A. Calarco. 2013. Heritable genome editing in *C. elegans* via a CRISPR-Cas9 system. *Nat. Methods*. 10:741–743. https://doi.org/10.1038/nmeth.2532

Fu, H., H. Zhou, X. Yu, J. Xu, J. Zhou, X. Meng, J. Zhao, Y. Zhou, A.D. Chisholm, and S. Xu. 2020. Wounding triggers MIRO-1 dependent mitochondrial fragmentation that accelerates epidermal wound closure through oxidative signaling. *Nat. Commun.* 11:1050. https://doi.org/10.1038/s41467-020-14885-x

Ghanta, K.S., and C.C. Mello. 2020. Melting dsDNA donor molecules greatly improves precision genome editing in *Caenorhabditis elegans*. *Genetics*. 216:643–650. https://doi.org/10.1534/genetics.120.303564

Gibson, D.G., L. Young, R.Y. Chuang, J.C. Venter, C.A. Hutchison III, and H.O. Smith. 2009. Enzymatic assembly of DNA molecules up to several hundred kilobases. *Nat. Methods*. 6:343–345. https://doi.org/10.1038/nmeth.1318

Glater, E.E., L.J. Megeath, R.S. Stowers, and T.L. Schwarz. 2006. Axonal transport of mitochondria requires milton to recruit kinesin heavy chain and is light chain independent. *J. Cell Biol.* 173:545–557. https://doi.org/10.1083/jcb.200601067

Glomb, O., G. Swaim, L.P. Munoz, C. Lovejoy, S. Sutradhar, J. Park, Y. Wu, S.E. Cason, E.L.F. Holzbaur, M. Hammarlund, et al. 2023. A kinesin-1 adaptor complex controls bimodal slow axonal transport of spectrin in *Caenorhabditis elegans*. *Dev Cell*. 58:1847–1863.e12. https://doi.org/10.1016/j.devcel.2023.08.031

Guo, X., G.T. Macleod, A. Wellington, F. Hu, S. Panchumarthi, M. Schoenfield, L. Marin, M.P. Charlton, H.L. Atwood, and K.E. Zinsmaier. 2005. The GTPase dMiro is required for axonal transport of mitochondria to *Drosophila* synapses. *Neuron*. 47:379–393. https://doi.org/10.1016/j.neuron.2005.06.027

Guo, Y., D. Li, S. Zhang, Y. Yang, J.J. Liu, X. Wang, C. Liu, D.E. Milkie, R.P. Moore, U.S. Tulu, et al. 2018. Visualizing intracellular organelle and cytoskeletal interactions at nanoscale resolution on millisecond timescales. *Cell*. 175:1430–1442.e17. https://doi.org/10.1016/j.cell.2018.09.057

Gutnick, A., M.R. Banghart, E.R. West, and T.L. Schwarz. 2019. The light-sensitive dimerizer zapalog reveals distinct modes of immobilization for axonal mitochondria. *Nat. Cell Biol.* 21:768–777. https://doi.org/10.1038/s41556-019-0317-2

He, S., A. Cuentas-Condori, and D.M. Miller III. 2019. NATF (native and tissue-specific fluorescence): A strategy for bright, tissue-specific GFP labeling of native proteins in *Caenorhabditis elegans*. *Genetics*. 212:387–395. https://doi.org/10.1534/genetics.119.302063

Hendricks, A.G., E. Perlson, J.L. Ross, H.W. Schroeder III, M. Tokito, and E.L. Holzbaur. 2010. Motor coordination via a tug-of-war mechanism drives bidirectional vesicle transport. *Curr. Biol.* 20:697–702. https://doi.org/10.1016/j.cub.2010.02.058

Hill, S.E., K.J. Kauffman, M. Krout, J.E. Richmond, T.J. Melia, and D.A. Colón-Ramos. 2019. Maturation and clearance of autophagosomes in neurons depends on a specific cysteine protease isoform, ATG-4.2. *Dev. Cell.* 49:251–266.e8. https://doi.org/10.1016/j.devcel.2019.02.013

Holm, L., A. Laiho, P. Törönen, and M. Salgado. 2023. DALI shines a light on remote homologs: One hundred discoveries. *Protein Sci.* 32:e4519. https://doi.org/10.1002/pro.4519

Hurd, D.D., and W.M. Saxton. 1996. Kinesin mutations cause motor neuron disease phenotypes by disrupting fast axonal transport in *Drosophila*. *Genetics*. 144:1075–1085. https://doi.org/10.1093/genetics/144.3.1075

Ivannikov, M.V., M. Sugimori, and R.R. Llinás. 2013. Synaptic vesicle exocytosis in hippocampal synaptosomes correlates directly with total mitochondrial volume. *J. Mol. Neurosci.* 49:223–230. https://doi.org/10.1007/s12031-012-9848-8

Jiang, R. 2021. An in vitro reconstitution investigation into the kinetic mechanisms underlying kinesin-based vesicle transport. Dissertation. ProQuest. The Pennsylvania State University, State College, PA. 144 pp.

Jumper, J., R. Evans, A. Pritzel, T. Green, M. Figurnov, O. Ronneberger, K. Tunyasuvunakool, R. Bates, A. Žídek, A. Potapenko, et al. 2021. Highly accurate protein structure prediction with AlphaFold. *Nature*. 596:583–589. https://doi.org/10.1038/s41586-021-03819-2

Kang, J.S., J.H. Tian, P.Y. Pan, P. Zald, C. Li, C. Deng, and Z.H. Sheng. 2008. Docking of axonal mitochondria by syntaphilin controls their mobility and affects short-term facilitation. *Cell*. 132:137–148. https://doi.org/10.1016/j.cell.2007.11.024

Kelliher, M.T., Y. Yue, A. Ng, D. Kamiyama, B. Huang, K.J. Verhey, and J. Wildonger. 2018. Autoinhibition of kinesin-1 is essential to the dendrite-specific localization of Golgi outposts. *J. Cell Biol.* 217:2531–2547. https://doi.org/10.1083/jcb.201708096

Klassen, M.P., and K. Shen. 2007. Wnt signaling positions neuromuscular connectivity by inhibiting synapse formation in *C. elegans*. *Cell*. 130:704–716. https://doi.org/10.1016/j.cell.2007.06.046

Kwon, S.K., R. Sando III, T.L. Lewis, Y. Hirabayashi, A. Maximov, and F. Polleux. 2016. LKB1 regulates mitochondria-dependent presynaptic calcium clearance and neurotransmitter release properties at excitatory synapses along cortical axons. *PLoS Biol.* 14:e1002516. https://doi.org/10.1371/journal.pbio.1002516

Leduc, C., O. Campàs, K.B. Zeldovich, A. Roux, P. Jolimaitre, L. Bourel-Bonnet, B. Goud, J.F. Joanny, P. Bassereau, and J. Prost. 2004. Cooperative extraction of membrane nanotubes by molecular motors. *Proc. Natl. Acad. Sci. USA*. 101:17096–17101. https://doi.org/10.1073/pnas.0406598101

Lewis, T.L. Jr., G.F. Turi, S.K. Kwon, A. Losonczy, and F. Polleux. 2016. Progressive decrease of mitochondrial motility during maturation of cortical axons in vitro and in vivo. *Curr. Biol.* 26:2602–2608. https://doi.org/10.1016/j.cub.2016.07.064

López-Doménech, G., C. Covill-Cooke, D. Ivankovic, E.F. Halff, D.F. Sheehan, R. Norkett, N. Birsa, and J.T. Kittler. 2018. Miro proteins coordinate microtubule- and actin-dependent mitochondrial transport and distribution. *EMBO J.* 37:321–336. https://doi.org/10.15252/embj.201696380

López-Doménech, G., N.F. Higgs, V. Vaccaro, H. Roš, I.L. Arancibia-Cárcamo, A.F. MacAskill, and J.T. Kittler. 2016. Loss of dendritic complexity precedes neurodegeneration in a mouse model with disrupted mitochondrial distribution in mature dendrites. *Cell Rep.* 17:317–327. https://doi.org/10.1016/j.celrep.2016.09.004

Macaskill, A.F., J.E. Rinholm, A.E. Twelvetrees, I.L. Arancibia-Carcamo, J. Muir, A. Fransson, P. Aspenstrom, D. Attwell, and J.T. Kittler. 2009. Miro1 is a calcium sensor for glutamate receptor-dependent localization of mitochondria at synapses. *Neuron*. 61:541–555. https://doi.org/10.1016/j.neuron.2009.01.030

Nguyen, T.T., S.S. Oh, D. Weaver, A. Lewandowska, D. Maxfield, M.H. Schuler, N.K. Smith, J. Macfarlane, G. Saunders, C.A. Palmer, et al. 2014. Loss of Miro1-directed mitochondrial movement results in a novel murine model for neuron disease. *Proc. Natl. Acad. Sci. USA*. 111:E3631–E3640. https://doi.org/10.1073/pnas.1402449111

Pilling, A.D., D. Horiuchi, C.M. Lively, and W.M. Saxton. 2006. Kinesin-1 and Dynein are the primary motors for fast transport of mitochondria in *Drosophila* motor axons. *Mol. Biol. Cell.* 17:2057–2068. https://doi.org/10.1091/mbc.e05-06-0526

Rai, A., D. Pathak, S. Thakur, S. Singh, A.K. Dubey, and R. Mallik. 2016. Dynein clusters into lipid microdomains on phagosomes to drive rapid transport toward lysosomes. *Cell*. 164:722–734. https://doi.org/10.1016/j.cell.2015.12.054

Rawson, R.L., L. Yam, R.M. Weimer, E.G. Bend, E. Hartwieg, H.R. Horvitz, S.G. Clark, and E.M. Jorgensen. 2014. Axons degenerate in the absence of mitochondria in *C. elegans*. *Curr. Biol.* 24:760–765. https://doi.org/10.1016/j.cub.2014.02.025

Rui, Y., P. Tiwari, Z. Xie, and J.Q. Zheng. 2006. Acute impairment of mitochondrial trafficking by beta-amyloid peptides in hippocampal neurons. *J. Neurosci.* 26:10480–10487. https://doi.org/10.1523/JNEUROSCI.3231-06.2006

Schnitzer, M.J., K. Visscher, and S.M. Block. 2000. Force production by single kinesin motors. *Nat. Cell Biol.* 2:718–723. https://doi.org/10.1038/35036345

Smit-Rigter, L., R. Rajendran, C.A. Silva, L. Spierenburg, F. Groeneweg, E.M. Ruimschotel, D. van Versendaal, C. van der Togt, U.T. Eysel, J.A. Heimel, et al. 2016. Mitochondrial dynamics in visual cortex are limited in vivo and not affected by axonal structural plasticity. *Curr. Biol.* 26:2609–2616. https://doi.org/10.1016/j.cub.2016.07.033

Söding, J., A. Biegert, and A.N. Lupas. 2005. The HHpred interactive server for protein homology detection and structure prediction. *Nucleic Acids Res.* 33:W244–W248. https://doi.org/10.1093/nar/gki408

Song, Y., P. Huang, X. Liu, Z. Zhao, Y. Wang, B. Cui, and L. Duan. 2022. Light-inducible deformation of mitochondria in live cells. *Cell Chem. Biol.* 29:109–119.e3. https://doi.org/10.1016/j.chembiol.2021.05.015

Stavoe, A.K., and D.A. Colón-Ramos. 2012. Netrin instructs synaptic vesicle clustering through Rac GTPase, MIG-10, and the actin cytoskeleton. *J. Cell Biol.* 197:75–88. https://doi.org/10.1083/jcb.201110127

Stavoe, A.K., J.C. Nelson, L.A. Martínez-Velázquez, M. Klein, A.D. Samuel, and D.A. Colón-Ramos. 2012. Synaptic vesicle clustering requires a distinct MIG-10/Lamellipodin isoform and ABI-1 downstream from Netrin. *Genes Dev.* 26:2206–2221. https://doi.org/10.1101/gad.193409.112

Stowers, R.S., L.J. Megeath, J. Górska-Andrzejak, I.A. Meinertzhagen, and T.L. Schwarz. 2002. Axonal transport of mitochondria to synapses depends on milton, a novel *Drosophila* protein. *Neuron.* 36:1063–1077. https://doi.org/10.1016/S0896-6273(02)01094-2

Sun, T., H. Qiao, P.Y. Pan, Y. Chen, and Z.H. Sheng. 2013. Motile axonal mitochondria contribute to the variability of presynaptic strength. *Cell Rep.* 4:413–419. https://doi.org/10.1016/j.celrep.2013.06.040

Sure, G.R., A. Chatterjee, N. Mishra, V. Sabharwal, S. Devireddy, A. Awasthi, S. Mohan, and S.P. Koushika. 2018. UNC-16/JIP3 and UNC-76/FEZ1 limit the density of mitochondria in *C. elegans* neurons by maintaining the balance of anterograde and retrograde mitochondrial transport. *Sci. Rep.* 8:8938. https://doi.org/10.1038/s41598-018-27211-9

Szpankowski, L., S.E. Encalada, and L.S. Goldstein. 2012. Subpixel colocalization reveals amyloid precursor protein-dependent kinesin-1 and dynein association with axonal vesicles. *Proc. Natl. Acad. Sci. USA.* 109: 8582–8587. https://doi.org/10.1073/pnas.1120510109

Tang, Y., and R.S. Zucker. 1997. Mitochondrial involvement in post-tetanic potentiation of synaptic transmission. *Neuron.* 18:483–491. https://doi.org/10.1016/S0896-6273(00)81248-9

Taylor, S.R., G. Santpere, A. Weinreb, A. Barrett, M.B. Reilly, C. Xu, E. Varol, P. Oikonomou, L. Glenwinkel, R. McWhirter, et al. 2021. Molecular topography of an entire nervous system. *Cell.* 184:4329–4347.e23. https://doi.org/10.1016/j.cell.2021.06.023

van Spronsen, M., M. Mikhaylova, J. Lipka, M.A. Schlager, D.J. van den Heuvel, M. Kuijpers, P.S. Wulf, N. Keijzer, J. Demmers, L.C. Kapitein, et al. 2013. TRAK/Milton motor-adaptor proteins steer mitochondrial trafficking to axons and dendrites. *Neuron.* 77:485–502. https://doi.org/10.1016/j.neuron.2012.11.027

Varadi, M., S. Anyango, M. Deshpande, S. Nair, C. Natassia, G. Yordanova, D. Yuan, O. Stroe, G. Wood, A. Laydon, et al. 2022. AlphaFold protein structure database: Massively expanding the structural coverage of protein-sequence space with high-accuracy models. *Nucleic Acids Res.* 50:D439–D444. https://doi.org/10.1093/nar/gkab1061

Verbrugge, S., S.M. van den Wildenberg, and E.J. Peterman. 2009. Novel ways to determine kinesin-1's run length and randomness using fluorescence microscopy. *Biophys. J.* 97:2287–2294. https://doi.org/10.1016/j.bpj.2009.08.001

Verstreken, P., C.V. Ly, K.J. Venken, T.W. Koh, Y. Zhou, and H.J. Bellen. 2005. Synaptic mitochondria are critical for mobilization of reserve pool vesicles at *Drosophila* neuromuscular junctions. *Neuron.* 47:365–378. https://doi.org/10.1016/j.neuron.2005.06.018

Wang, X., G. Perry, M.A. Smith, and X. Zhu. 2010. Amyloid-beta-derived diffusible ligands cause impaired axonal transport of mitochondria in neurons. *Neurodegener. Dis.* 7:56–59. https://doi.org/10.1159/000283484

Wang, X., D. Winter, G. Ashrafi, J. Schlehe, Y.L. Wong, D. Selkoe, S. Rice, J. Steen, M.J. LaVoie, and T.L. Schwarz. 2011. PINK1 and Parkin target Miro for phosphorylation and degradation to arrest mitochondrial motility. *Cell.* 147:893–906. https://doi.org/10.1016/j.cell.2011.10.018

White, J.G., E. Southgate, J.N. Thomson, and S. Brenner. 1986. The structure of the nervous system of the nematode *Caenorhabditis elegans*. *Philos. Trans. R. Soc. Lond. B Biol. Sci.* 314:1–340. https://doi.org/10.1098/rstb.1986.0056

Yan, J., D.L. Chao, S. Toba, K. Koyasako, T. Yasunaga, S. Hirotsune, and K. Shen. 2013. Kinesin-1 regulates dendrite microtubule polarity in *Caenorhabditis elegans*. *Elife.* 2:e00133. https://doi.org/10.7554/eLife.00133

Zhao, X.L., W.A. Wang, J.X. Tan, J.K. Huang, X. Zhang, B.Z. Zhang, Y.H. Wang, H.Y. YangCheng, H.L. Zhu, X.J. Sun, and F.D. Huang. 2010. Expression of beta-amyloid induced age-dependent presynaptic and axonal changes in *Drosophila*. *J. Neurosci.* 30:1512–1522. https://doi.org/10.1523/JNEUROSCI.3699-09.2010

Zhao, Y., E. Song, W. Wang, C.H. Hsieh, X. Wang, W. Feng, X. Wang, and K. Shen. 2021. Metaxins are core components of mitochondrial transport adaptor complexes. *Nat. Commun.* 12:83. https://doi.org/10.1038/s41467-020-20346-2

Supplemental material
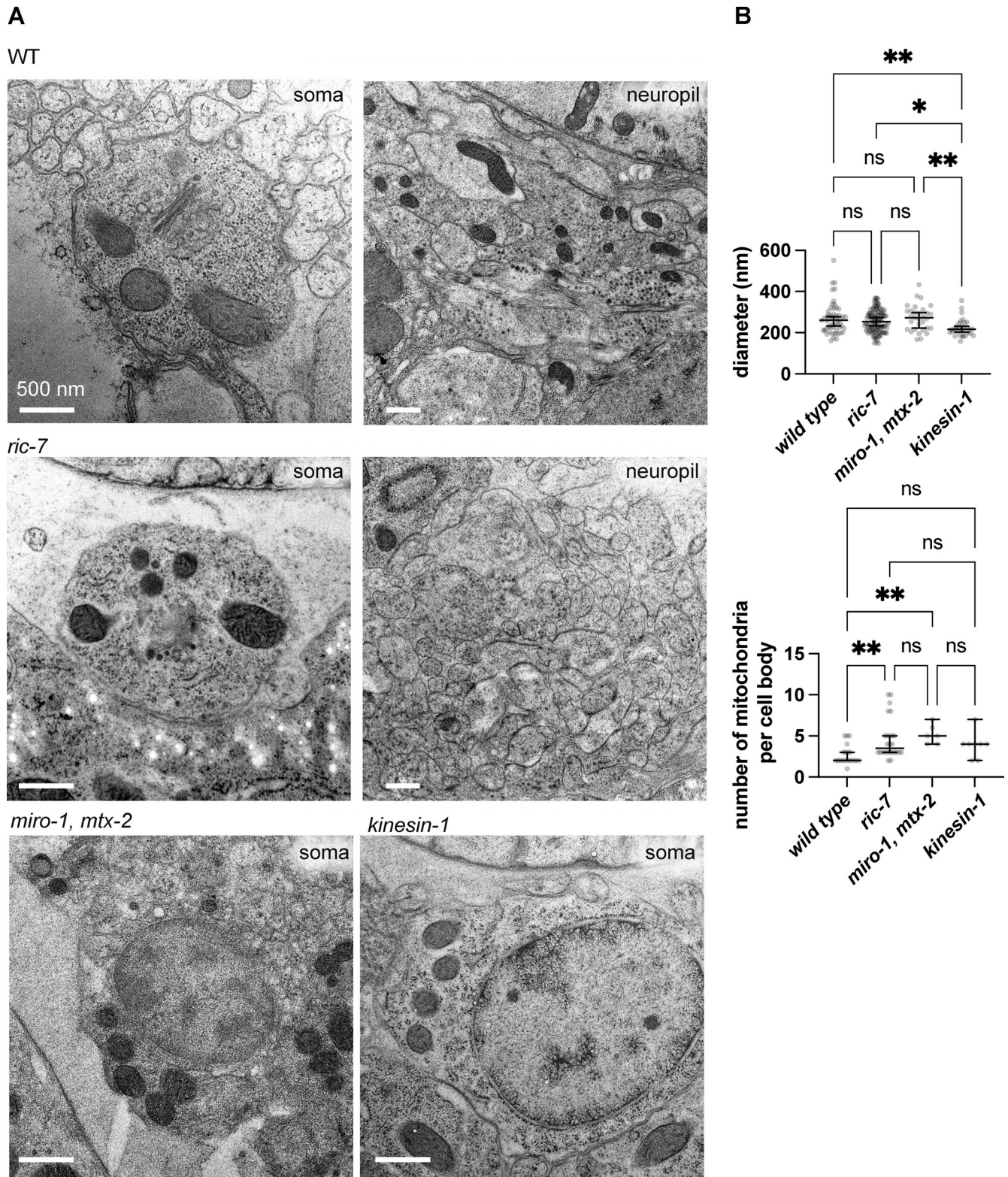
Figure S1. **Mitochondria are absent from the neuropil in *ric-7* mutants. (A)** Representative images of the soma and/or neuropil area in WT, *ric-7*, *miro-1*; *mtx-2* and *kinesin-1* mutants under electron microscopy. **(B)** Quantification of mitochondria diameter and number in the soma in WT, *ric-7*, *miro-1*; *mtx-2* and *kinesin-1* mutants. Each dot represents an individual mitochondrion in the upper panel and an individual cell body in the lower panel. Number of animals = 2 for each genotype (one-way ANOVA with multiple comparisons).
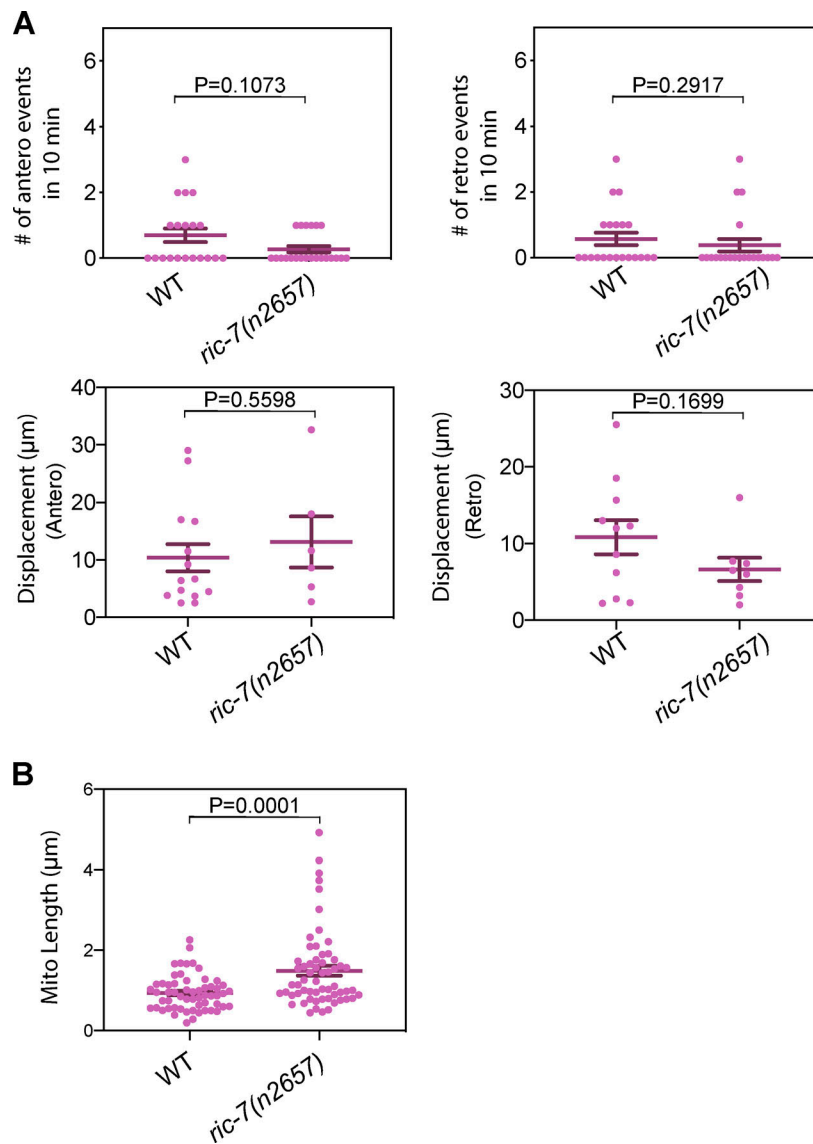
Figure S2. **Mitochondria trafficking in the DA9 dendrite is not affected in *ric-7* mutant. (A)** Quantification of mitochondria trafficking events in DA9 dendrite. Upper panels: Each dot represents the number of observed trafficking events in each 10-minute-long video. Lower panels: Each dot represents one trafficking event. The total number of videos: WT = 20, *ric-7* = 22, pooled from four independent experiments. (Mann–Whitney test for upper panels and two-sided *t* test for lower panels.) **(B)** Dendritic mitochondria length quantified from still images. Each data point represents one mitochondrion. Same datasets as in Fig. 3 F (two-sided *t* test).
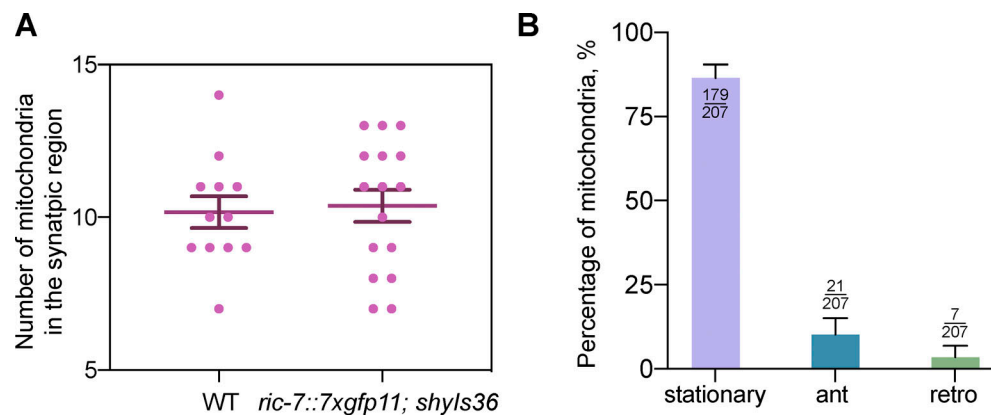
Figure S3. **Functional validation of RIC-7::7xSplitGFP. (A)** Mitochondria distribution in the axon is not affected when RIC-7 is tagged with 7xSplitGFP at its C-terminus. Each data point represents one animal. Error bars represent SEM. Total number of animals: WT = 12, *ric-7::7xgfp11; shyIs36* = 16. Data of *ric-7::7xgfp11; shyIs36* are pooled from two independent experiments, and WT data is duplicated from Fig. 3 E (two-sided *t* test). **(B)** Percentage of mobile mitochondria in the DA9 axon. Events in the synaptic region are quantified and the numbers are indicated at the top of each bar. Same datasets as in Fig. 4 G. Error bars represent 95% confidence intervals.

Figure S4. **Structure/function analysis of RIC-7. (A)** Transcript expression level of *ric-7*, *itr-1*, and *mig-13* in DA9 (threshold = 2) (Taylor et al., 2021). *ric-7* is so lowly expressed that it's not detected in DA9. **(B)** Schematic representations of the three splicing isoforms of *ric-7*. **(C)** Transcript expression level of the three splicing isoforms of *ric-7* in different neurons. Note that *ric-7b* has a relatively higher expression than the other two isoforms. **(D)** Representative images showing the localization of 1–99 aa and 100–470 aa in the cell body expressed as transgenes driven by the promoter of *Pmig-13* in different genotypes (see Materials and methods). **(E)** Representative images showing the localization of 1–99 aa and 100–470 aa in the dendrite expressed as transgenes driven by the promoter of *Pmig-13* in *ric-7* mutant animals. **(F)** Quantification of the percentage of mitochondria associated with EGFP signals. Number of mitochondria counted are indicated at the top of each bar. Error bars represent 95% confidence intervals. Total number of animals is seven for each condition. **P < 0.01 (Fisher's exact test).

A

```
Q ss_pred            ccCCCCcchHHHHHHHHcCCCCcchHHHHHHHh--hcceeeeeCCCCcCChHHHHHHHHHHHHHHcCCccccccCCHHHHHH
Q Q_1261352    472   KFAPKMSRDLMVMACEIFQPYSPPFRDLQTIYH--KRRLKRVAVPSVTESNESCVSLFMRSALYHKCSLLRDATWSIIEK    549 (709)
Q Consensus    472   ~~~~~~TRDLMV~A~E~F~p~S~qfK~lq~LY~--rrRlrRIg~~~~~~~~e~~L~~~L~s~lyh~~~~f~~s~~~~ieK    549 (709)
                     +++|++.+||+.||++||||+|+|++.|||||+  .++|++||+|||||||  ||||+|||+|++|+++|.|.+..++.+
T Consensus     2    ~~sv~~~vdi~~Y~~~eWkG~T~ka~~irkgY~~i~~~~~~lRrvRgDNYC~~aLRAtLFQ~Ls~~~~lp~w~~~~~~~~    79 (268)
T 6I9C_A         2    PLSVAPEMDIMDYCKKEWRGNTQKATCMKMGYEEVSQKFTSIRRVRGDNYC~~ALRATLFQAMSQAVGLPPWLQDPELML   79 (268)
T ss_dssp             CCSBCCCEEHHHHHHHHCCSSCHHHHHHHHHHHHHTTTCSEEECBCCSTTH~~HHHHHHHHHHHTCSSCCHHHHCTHHHH
T ss_pred             CCccCchHHHHHHHHHHhCCCCHHHHHHHHHHHHHHHHcccccccCCCChh~~HHHHHHHHHHHcCCCCCHHHcCHHHhh


Q ss_pred            HHHHHhhcceeecCCCCCh------------HHHHHHHHHHHHHcCCC-C-----------CC--CCHHHHHHHHHHHH
Q Q_1261352    550   RFDNAVQECDFMNKWPGYSP------------SSMRKDLKKLHDLASTDS-L-----------SG--LEEDHHKAYQVLM    603 (709)
Q Consensus    550   ~~~~~lsecdFl~~W~~~~~~~~~~~~~~~~~~mr~~L~~Lwdl~~~~~~l~~~~~~~~~~~~~~ve~~~iea~~~lL~    603 (709)
                     +|++|.++|+||+||+|+.+          ..||++|+++|+++++++ .          ++  +|++|||||||||
T Consensus     80   lp~~l~~~~~wi~qW~F~~~~~~~~~~~~~~l~~cL~~L~~~w~~~~~~~~~~R~~~c~~Lf~~~~~E~~l~EAvKllM    159 (268)
T 6I9C_A         80   LPEKLISKYNWIKQWKLGLKFDGKNEDLVDKIKESLTLLRKKWAGLAEMRTAEARQIACDELFTNEAEEYSLYEAVKFLM   159 (268)
T ss_dssp             HHHHHHHHHCGGGGGCCCC--------CHHHHHHHHHHHHHHHHTCSSHHHHHHHHHHCSSSHHHHHHHHHHHH
T ss_pred             HhHHHHhcCCChHhceeecccCCCCCcCHHHHHHHHHHHHHHHHHHHHcCCCHHHHHHHHHHHcCCCHHHHHHHHHHHHHHH


Q ss_pred            HHHHHHHHHHHHHcCc----cchhhhcC---CCHHHHHHH-HHHcCCCCChHHHHHHHHHHHHHCCeEEEEEccccccCCCc
Q Q_1261352    604   VLEAKRAYDERLAGL----FCEDWFNV---DSPADIFKI-LVDRGDDDLPPKILWNILCRISGVSIEIIDARGLSEHPKI    675 (709)
Q Consensus    604   VL~a~~~fe~~~ag~----f~~~~F~~~~~~nP~~I~~~-l~~~~~~~p~~~~~~LL~~t~~i~iEi~D~~~~s~~~~~    675 (709)
                     |++|++||+++++|+     |||+|||| .+|++||+| ||+|++++|||||||||||||||++||+|+||+++++|||+
T Consensus    160   L~~AieL~~~~~g~~VP~F~~lLFARdTS~~P~~fm~NHLN~VG~s~GLEQVEM~LLgytL~~tI~V~Rl~~~~~edFi    239 (268)
T 6I9C_A        160   LNRAIELYNDKEKGKEVPFFSVLLFARDTSNDPGQLLRNHLNQVRHTGGLEQVEMFLLAYAVRHTIQVYRLSKYNTEEFI   239 (268)
T ss_dssp             HHHHHHHHHHHTTCCCCHHHHHHHSTTCSSHHHHCCCCCTCCTTTCCCCHHHHHHHHHHTCEEEEEEGGGTTSGGGE
T ss_pred             HHHHHHHHHHHCCCCCCceeeeecccCCCCCHHHHHHHHhhhcccCChhHHHHHHHHHHHHcCeEEEEEeeccCCccEE


Q ss_pred            cccCCCCCCCCCCCeeeEeccCCCCc
Q Q_1261352    676   NRFSASASPISAPCLTWLRLGKRPV    700 (709)
Q Consensus    676   ~r~st~~~~~~~p~lt~Lk~~~~~    700 (709)
                     ++|||  +++++||+|+|||||||||
T Consensus    240   ~~YPd~~~~~~wp~v~LitEddrHY    263 (268)
T 6I9C_A        240   TVYPT-DPPKDWPVVTLIAEDDRHY   263 (268)
T ss_dssp             EEESS-SCCTTSCEEEEEESSSSCE
T ss_pred             EEecC-CCCCCCCeeEEEEeCCCcc
```

B

Figure S5. **Human Otulin or OtulinL, or the C-term domain of RIC-7 cannot rescue mitochondria localization in *ric-7* mutant. (A)** Protein remote homology detection for RIC-7b using HHPred (https://toolkit.tuebingen.mpg.de/tools/hhpred). Human proteome was selected as the search database. The top two hits were OtulinL and Otulin. Sequence alignment between RIC-7b and Otulin is shown in this figure. Note the high similarity of the secondary structures of the Query (Q1261352: RIC-7b) and Target (T 619C_A: Otulin). SS_Pred denote the PSI-PRED secondary structure prediction and "ss_dssp" is the actual secondary structure determined by the program DSSP. Quality of the column–column match: | very good, + good, · neutral, – bad, and = very bad. **(B)** Representative images showing mitochondria localization in *ric-7* mutant animals expressing the human Otulin or OtulinL, or the C-term domain (471–709 aa) of RIC-7 driven by a pan-neuronal promoter from a single copy insertion.

Video 1. **Mitochondria trafficking in AIY neuron in a WT animal.** Live cell imaging was performed after mitochondria are photoconverted in the cell body in a WT animal. Images were taken every 110 s for 104 min. The video is played at 1,200× speed real time.

Video 2. **Mitochondria trafficking in AIY neuron in an *miro-1* animal.** Live cell imaging was performed after mitochondria are photoconverted in the cell body in an *miro-1* animal. Images were taken every 5 min for 340 min. The video is played at 1,200× speed real time.

Video 3. **RIC-7::7xSplitGFP signals are associated with anterograde but not retrograde trafficking mitochondria.** Ventral view of an axon segment that is proximal to the cell body. RIC-7::7xSplitGFP in green and mito::TagRFP in magenta. The circle indicates the cell body that is out of focus, with the axon to the right. One mitochondrion is transported back to the cell body without RIC-7::7xSplitGFP, whereas another mitochondrion transporting from the cell body into the axon is associated with RIC-7::7xSplitGFP. Images were taken every 10 s and the play rate is 5 fps.

Video 4. **RIC-7::7xSplitGFP are enriched at the leading end of mitochondria that transported anterogradely in the axon.** Dorsal view of the synaptic region in the axon. Distal end is to the left. RIC-7::7xSplitGFP in green and mito::TagRFP in magenta. A mitochondrion is moving anterogradely, with RIC-7::7xSplitGFP at the leading end. Images were taken every 10 s and the play rate is 5 fps. See Fig. 4 I for the still images.

Video 5. **RIC-7::7xSplitGFP are enriched at the leading end of mitochondria that enter the axon.** Ventral view of the cell body with the axon to the right. The dendrite is out-of-focus. RIC-7::7xSplitGFP in green and mito::TagRFP in magenta. This video shows two mitochondria that first extend into the axon, followed by fission and transport, with RIC-7::7xSplitGFP at the leading end. Images were taken every 10 s and play rate is 5 fps. See Fig. 4 K for the still images. Images were taken every 10 s and the play rate is 5 fps.

Video 6. **RIC-7::7xSplitGFP are not associated with mitochondria that enter the dendrite.** Ventral view of the cell body with the dendrite to the right and the axon to the left. The axon is slightly out of focus. RIC-7::7xSplitGFP in green and mito::TagRFP in magenta. One mitochondrion enters the dendrite without RIC-7::7xSplitGFP. Images were taken every 10 s and the play rate is 5 fps.

Video 7. **Kinesin-1::3xSplitGFP (UNC-116::3xSplitGFP) are enriched at the leading end of mitochondria that transported anterogradely in the axon.** Lateral view of the synaptic region in the axon. Distal end is to the left. kinesin-1::3xSplitGFP in green and mito::TagRFP in magenta. A mitochondrion is moving anterogradely, with kinesin-1::3xSplitGFP at the leading end most of the time. Note the presence of a cytoplasmic pool of kinesin-1::3xSplitGFP. Images were taken every 10 s and the play rate is 5 fps.

Video 8. **RIC-7::7xSplitGFP are associated with mitochondria that enter the axon in *mtx-2* mutant, but is not enriched at the leading end.** Ventral view of the cell body with the axon to the right. The cell body is out-of-focus, which is indicated by the asterisk. RIC-7::7xSplitGFP in green and mito::TagRFP in magenta. RIC-7::7xSplitGFP is associated with the mitochondrion that moves anterogradely, but no longer accumulates at the leading end. Images were taken every 10 s and the play rate is 5 fps.

Video 9. **3D structure comparison by Dali.** The structure of RIC-7b predicted by Alphafold was searched against the human proteome on the Dali server (ekhidna2.biocenter.helsinki.fi/dali/). The top two hits were OtulinL and Otulin. 3D structure alignment was shown in this video, with RIC-7b in green and Otulin in orange. The predicted 3D structure of RIC-7b C-term is highly similar to that of Otulin.

Provided online are five tables. Table S1 lists strains used in this study. Table S2 lists plasmids used in this study. Table S3 lists gRNA sequences used in this study. Table S4 lists genotyping primers for CRISPR alleles used in this study. Table S5 shows allele sequences.